Fachhochschule Vorarlberg
Vorarlberg University of Applied Sciences

Simulation and Characterization of a Miniaturized Planar Coil

Master's in Mechatronics

A Thesis Submitted in Partial Fulfillment of the
Requirements for the Degree of
Master of Science in Engineering, MSc

Dornbirn, August 2009

Submitted to
Johannes Edlinger and
Johannes Steinschaden

Submitted by
Florian Hämmerle

Carried out at the
Research Centre for Microtechnology

Abstract

The focus of this thesis lies on the experimental characterization and simulation based on the finite element method (FEM) of a planar miniaturized coil. The geometry of planar coils is compatible with manufacturing processes that are used for integrated circuit production. Working prototypes of a miniaturized planar coil for radio frequency identification (RFID) were realized at the Research Centre for Microtechnology (FZMT) at the Vorarlberg University of Applied Sciences as part of the "Polyhybrid" project funded by the Interreg IIIA program of the European Union. As a next step the present planar coils shall be further miniaturized and optimized. In this thesis the use of FEM simulations for the design and optimization of the planar coils was investigated.

The equivalent circuit parameters (coil inductance L, wire resistance R_L) of the present planar spiral coil were measured at 13.56 MHz. The measurements were performed using a vector network analyzer and a specially designed probe configuration. As the material parameters needed for the FEM simulations were unknown, the relative permeability and the volume resistivity of the conductor material (electroplated nickel) were independently measured.

The simulation method chosen to calculate the equivalent circuit parameters was to simulate the quasistatic magnetic field and the electric field separately. Results from 2D and 3D harmonic magnetic field simulations and 3D static electric field simulations were compared with results achieved by the Graz University of Technology to verify the results gathered by a commercial FEM program.

Using the exact coil geometry and the measured material parameters as an input for the simulations, it was possible to predict the coil inductance with an error of less than 4.5 % and the coil resistance with an error of less than 1 %. It was found that both, the 3D and 2D magnetic field simulations are useful tools in the design process of planar coils. Using the simulation method applied in this thesis the following goals shall be achieved in future work: Decrease the coil size and adapt the design to an optimum, increase the RFID operating distance, integrate a matching capacitance into the coil design and reduce time respectively costs of the development cycle.

Parts of the results of this thesis are to be published in the Compumag 2009 conference proceedings and/or the IEEE Transactions on Magnetics under the title "Calculation of Equivalent Circuit Parameters for a High-Frequency RFID Transponder".

Kurzfassung

Die vorliegende Arbeit behandelt das Thema "Simulation und Charakterisierung einer miniaturisierten Planarspule". Miniaturisierte Spulen werden in vielen Anwendungsbereichen verwendet. Aufgrund ihrer planaren Struktur können Fertigungsprozesse aus der Halbleiterindustrie für die Herstellung verwendet werden. Am Forschungszentrum Mikrotechnik (FZMT) der FH Vorarlberg werden funktionstüchtige Prototypen eines miniaturisierten RFID tags (radio frequency identification) hergestellt. Diese Entwicklung fand im Projekt "Polyhybrid" des Interreg IIIA Programms der EU statt. In weiterer Folge soll das bestehende Design weiter miniaturisiert werden und die Reichweite erhöht werden. In dieser Arbeit wird untersucht, ob elektromagnetische Finite Element Simulationen (FEM) als Unterstützung für die Entwicklung und Optimierung der Planarspulen geeignet sind.

Durch experimentelle Messungen wurden die Werte des Spulenersatzschaltbilds bei $13.56\,\mathrm{MHz}$ bestimmt. Die Messung erfolgte mit einen Vektor Netzwerkanalysator. Die Kontaktierung wurde mit einem eigens entwickelten Kontaktieraufbau bewerkstelligt. Da die für die FEM Simulationen benötigten Materialparameter nicht bekannt waren, wurden die relative Permeabilität und der spezifische Widerstand des Leitermaterials (galvanisch abgeschiedenes Nickel) bestimmt.

Zur Berechnung der Ersatzschaltbild-Parameter wurden Elektromagnetische FEM Simulationen verwendet. Als gewählte Näherung wurden das magnetische und das elektrische Feld getrennt voneinander berechnet. Die Ergebnisse der 2D und 3D Simulationen wurden mit Ergebnissen der TU Graz verglichen um die Ergebnisse des kommerziellen Programms zu verifizieren.

Unter Verwendung der exakten Spulengeometrie und der gemessenen Materialparameter war es möglich, den Spulenwiderstand auf $1\,\%$ genau zu berechnen. Die Induktivität wurde auf ca. $4.5\,\%$ genau bestimmt. Zusammenfassend kann gesagt werden, dass die elektromagnetischen 2D und 3D Simulationen geeignete Werkzeuge sind um den Entwicklungsablauf der Planarspulen zu unterstützen. Mit Hilfe der hier vorgestellten Simulationsmethodik sollen in Zukunft die folgenden Ziele erreicht werden: Miniaturisierung und Optimierung des Spulendesigns, erhöhen der RFID Reichweite, Integration einer Anpassungskapazität in das Spulendesign und Reduktion der Entwicklungszeiten und Kosten.

Teile der Ergebnisse dieser Arbeit werden im Tagungsbericht der Compumag 2009 bzw. in den IEEE Transactions on Magnetics unter dem Titel "Calculation of Equivalent Circuit Parameters for a High-Frequency RFID Transponder" publiziert.

Acknowledgement

Sworn Declaration

I hereby declare under oath that this master's thesis is the product of my own independent work. All content and ideas drawn directly or indirectly from external sources are indicated as such. The thesis has not been submitted to any other examining body and has not been published.

Dornbirn, August 25, 2009

Contents

Contents

1. Introduction

1.1. Motivation

Coils as inductances are used in nearly every area of electronic engineering. The standard way of introducing an inductance to an electronic circuit is to use discrete components. Since 1990 inductors have been directly fabricated on silicon wafers. [AB03] deals with various ways of integrating inductors and ICs directly on silicon. The coils used in RF-ICs are mostly planar coils with diameters in the range of some $100\,\mu$m. The achieved inductance values are in the range of nH.

The focus of the following thesis lies on the characterization of a discrete miniaturized coil which can be used in various fields of application e.g. RFID[1], wireless sensors or actuators. The main difference to silicon based on chip inductances is the physical size of the coils. That is, the size of the coils is of the order of some millimeters and not of the order of some $100\,\mu$m. Furthermore the studied coil geometry is designed for an operation frequency of $13.56\,$MHz and not for operation in the range of some GHz as the $13.56\,$MHz frequency range is an open standard for industrial applications.

The initial goal was to develop a miniaturized RFID tag. This project ("Polyhybrid") was funded by the INTERREG IIIA program. Its results can be viewed unter http://www.interreg.org. During the "Polyhybrid" project several questions came up. Some of them are:

- How can the operating distance of the RFID application be increased and what are the limits?

- Is there a possibility of including the tuning capacitance in the coil design?

- How adequate is the available coil geometry for use in a wireless sensor or in a wireless sensor network?

- What tradeoff can be made on the coil geometry, without loosing performance, to increase the process window for the production process?

The work of the following thesis deals with possibilities and methodologies that could be used as tools to answer some of the questions mentioned above.

---

[1]Radio Frequency IDentificaion

1.2. Thesis Problem and Approach

During the work of this thesis the planar coil shall be characterized using a commercial FEM[2] simulation software. The results of this simulation shall be validated by comparison with results achieved by the "IGTE[3]" department at the Graz University of Technology (http://www.igte.tugraz.at). In addition the material used to manufacture the coil shall be characterized and the results of the simulation are compared with measurement results. In summary this means:

1. Validation of the simulation method by comparing the simulation results with simulation results from IGTE department.

2. Characterization of the materials resulting from the coil manufacturing process.

3. Characterization of the coil equivalent circuit parameters via experimental measurements.

4. Simulation of the coils using the experimentally determined material parameters and comparing the results with the measurements.

---

[2]Finite Element Method
[3]Institute for Fundamentals and Theory in Electrical Engineering

2. Miniaturized Coils

During this chapter several possible coil geometries are shown and their miniaturization is discussed. Secondly the existing miniaturized coil geometry is presented and the fabrication process is explained in detail. Additionally the RFID application for the planar coil is presented in detail.

2.1. State of the Art

2.1.1. Various Coil Geometries

Inductors, respectively coils exist in various geometrical forms. In practice, different coil geometries are used for different applications. In the following, the coil geometries displayed in figure 2.1 are explained in detail.

(a) Solenoidal coil   (b) Toroidal coil   (c) Planar coil
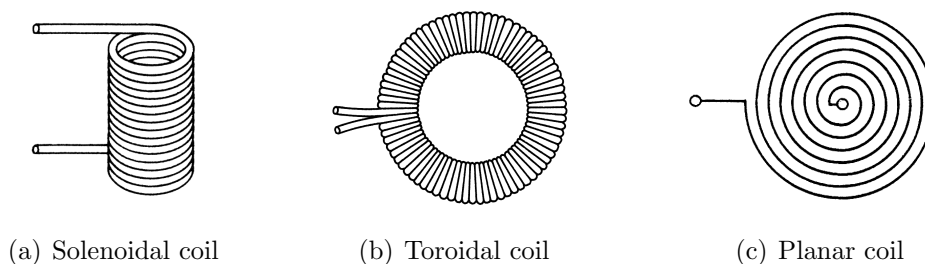
Figure 2.1.: Various coil geometries [Beu03, page 67]

Solenoidal Coil

The solenoidal coil see figure 2.1(a) is a very common coil geometry e.g. used for electromagnets or radio receiver antennas. Some characteristic properties of the solenoidal coil are:

- Easy production process using winding machines

- Possibility of adding a ferromagnetic core to enhance inductance

- Good characterization through empirical formulas

- High parasitic capacitance which limits maximum operation frequency

- High directionality of the magnetic field

Toroidal Coil

The toroidal coil see figure 2.1(b) on the preceding page is often used for high inductance discrete components. The most characteristic property is the very low magnetic leakage flux. Some characteristic properties are:

- Very low magnetic leakage flux

- Possibility of adding a ferromagnetic core to increase the inductance

- Complex fabrication process

- Concentration of magnetic flux inside the core

Planar Coil

Planar coils see figure 2.1(c) on the previous page, also named "spiral coils" or "planar spiral coils" , are widely used in printed circuit board (PCB) applications where the coil geometry can be integrated in the board design. Also on-chip inductances are mostly designed as planar coils. Characteristic properties are:

- High magnetic leakage flux

- Parasitic capacitance highly dependent on substrate material

- Adding effective magnetic core is difficult

- Planar geometry, suitable for fabrication processes compatible with IC-fabrication

2.1.2. Coil Miniaturization

The previous section shows geometrical possibilities of coil design. During miniaturization, the available fabrication technology and processes affect and limit the geometrical variability.

Fabrication technology in micro techniques is mostly based on "planar" fabrication steps. For the creation of 3-dimensional structures, more technology steps are necessary than for the fabrication of 2-dimensional structures. As costs directly increase with the number of technology steps, planar structures are preferred.

2.1.3. Miniaturization Examples

In literature various coil geometries and fabrication techniques can be found. [AA98] presents a solenoidal and toroidal coil with a micro-machined magnetic nickel core. Figure 2.2 shows the geometry of the solenoidal coil.
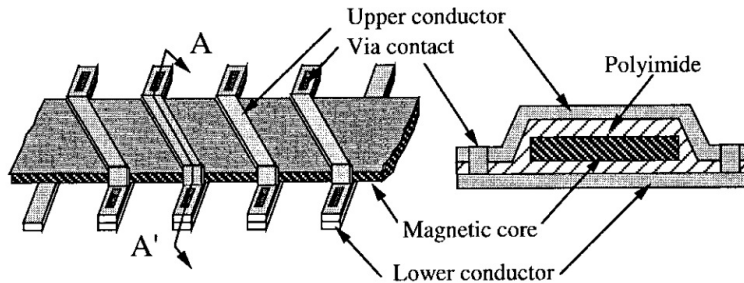
Figure 2.2.: Miniaturized Solenoidal Coil [AA98]

The geometrical size of the inductor shown in figure 2.2 is $4\,\text{mm} \times 1\,\text{mm} \times 120\,\mu\text{m}$. According to [AA98], an inductance value of $0.729\,\mu\text{H}$ was achieved at a quality factor of approximately 1.5 (at $1\,\text{MHz}$). Because of the highly permeable core, the inductance value is varying with frequency and decreasing significantly at frequencies above $1\,\text{MHz}$.

(a) Priciple Geometry   (b) Microimage
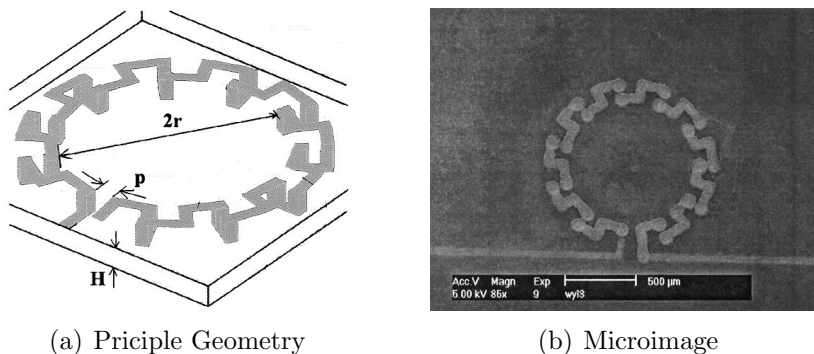
Figure 2.3.: Miniaturized Toroidal Coil [LSN$^+$04]

In [LSN$^+$04] the development of a miniaturized toroidal inductor is presented. An advantage of the toroidal geometry is the confined magnetic field which reduces eddy currents and the interference with metals or semiconducting materials. Figure 2.3 shows the miniaturized toroidal inductor. The achieved inductance value was $2.5\,\text{nH}$ below $10\,\text{GHz}$. The peak quality factor Q is 22 at $1.5\,\text{GHz}$.

The standard geometry for miniaturized coils is the planar spiral coil. Figure 2.4 on the following page illustrates a planar inductor. [NJS$^+$97] presents an implantable
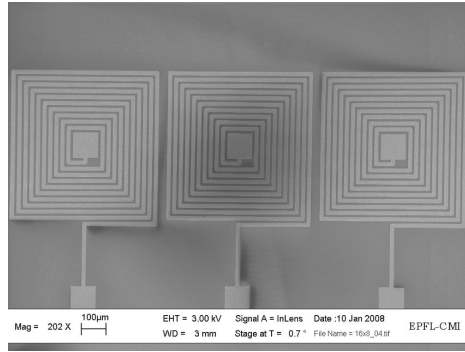
Figure 2.4.: Planar Coil Geometry [MMP08]

spiral planar coil with an outer diameter of $4.5\,\text{mm}$. The achieved inductance value is about $20\,\mu\text{H}$ with quality factor of 3. The self resonance frequency is about $3\,\text{MHz}$.

Each of the above presented coil geometries have advantages and disadvantages and are suitable for diverse applications. Within this thesis is brought into focus a planar spiral coil which is designed for use as an antenna for a near field coupling RFID-tag. This coil is presented in the following part.

2.2. Present Planar Coil Geometry

Figure 2.5 shows the design of the available planar coil. The coil measures $6\,\text{mm} \times 6\,\text{mm}$. The number of windings equals $N = 14$. The conductors have a rectangular cross section with height $h = 80\,\mu\text{m}$ and width $w = 30\,\mu\text{m}$. The insulation between the tracks has a thickness of $100\,\mu\text{m}$ and a width of $60\,\mu\text{m}$. In the following section the fabrication process is presented in detail.
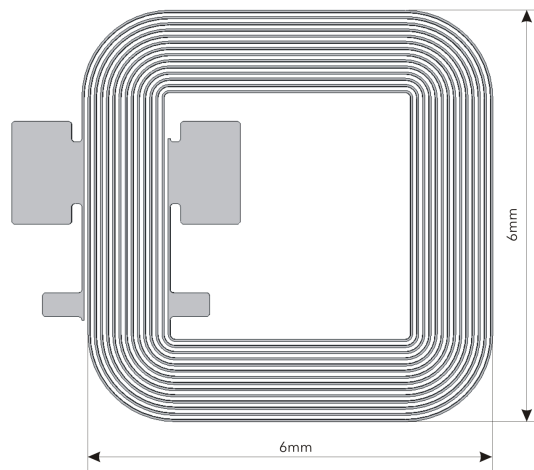
Figure 2.5.: Existing Planar Coil Design

2.2.1. Fabrication Process

The actual fabrication process is based on 100 mm glass wafers. With the current mask design, one wafer contains 88 coils. Figure 2.7 on the following page explains
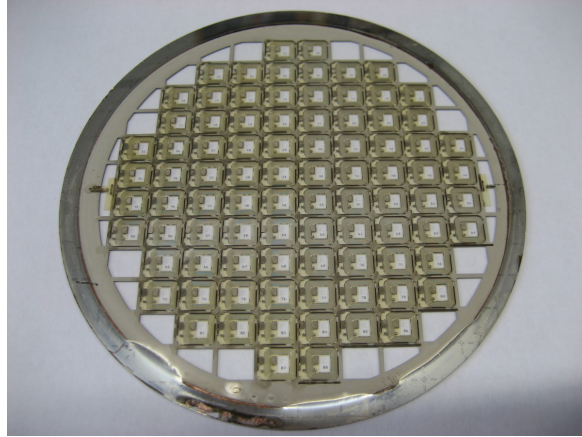
Figure 2.6.: Processed Wafer Containing 88 Coils

the production methodology in detail. At first the substrate (Pyrex) is coated with a multilayer seed layer via sputtering. Secondly, the seed layer is coated with a photoresist. After lithography the seed layer is patterned with wet etching. Thereafter the 100 μm thick layer of SU-8 photoresist is applied and structured. This layer of resist is used as a mold for the electroplating. Finally, the conductor is fabricated via nickel electroplating. The following enumeration summarizes the process flow also shown in figure 2.7 on the next page:

1. Thin film coating of the substrate (seed layer for the electroplating)

2. Structuring of the seed layer using photo lithography

3. 100 μm resist structuring as a mold for the electroplating

4. Nickel electroplating to achieve a thick conductor

The process parameters for the Nickel electroplating process are listed in the appendix A on page 87.

2.3. RFID Application

As already mentioned, the existing planar coil is designed for use as an antenna for an RFID Tag. Figure 2.8 on the next page shows the assembled RFID tag with the planar coil. The coil is used as the coupling antenna and as the carrier for the RFID chip. A 13.56 MHz RFID chip (Type: LEGIC MIM256) and a matching capacitor are mounted on the planar coil.

Seed Layer

Lithography

Seed Layer Structuring

SU-8 Application
and Lithography

Electroplating
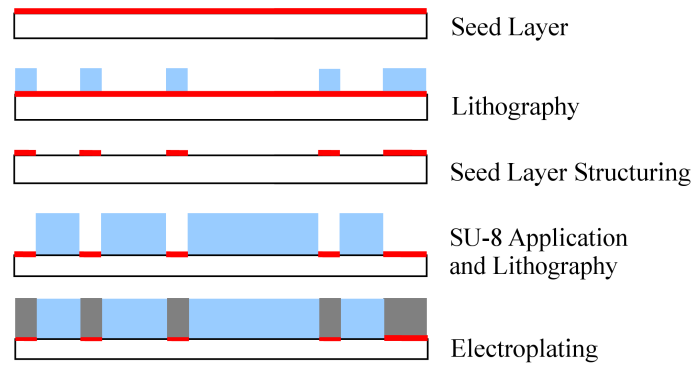
Figure 2.7.: Process Flow [CMP08]
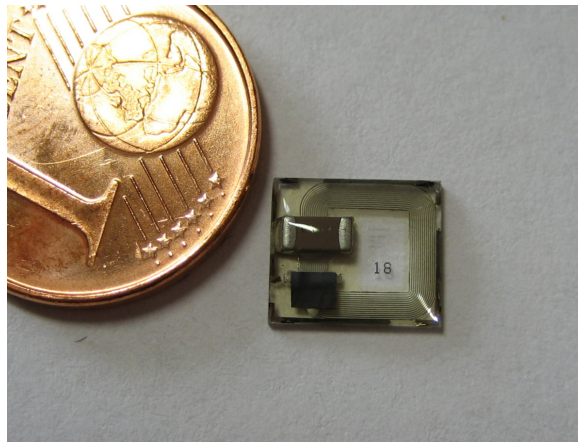
Figure 2.8.: Assembled RFID Tag with Planar Coil

2.3.1. Working principle

The RFID tag is designed to work in passive mode using inductive coupling. That is, the energy necessary for the communication is transmitted from the reader to the transponder. Figure 2.9 on the facing page shows the working principle of a passive RFID communication with a passive transponder. The reader produces a magnetic field with the transmission frequency of 13.56 MHz. If the transponder gets into this magnetic field, the transponder gets into resonance and the induced voltage at the RFID chip increases. If the voltage exceeds the working voltage, the chip starts to work. The communication via reader and transponder is realized through load modulation. A load resistor is switched on and off on the transponder side. The switching has an impact on the magnetic field and can therefore be recognized on the reader side.

The "transformer like" coupling strength between the reader and transponder coil is dependent on the distance between the coils, the operating frequency and the inductance values of the coils. The requirements for high operating distance using small
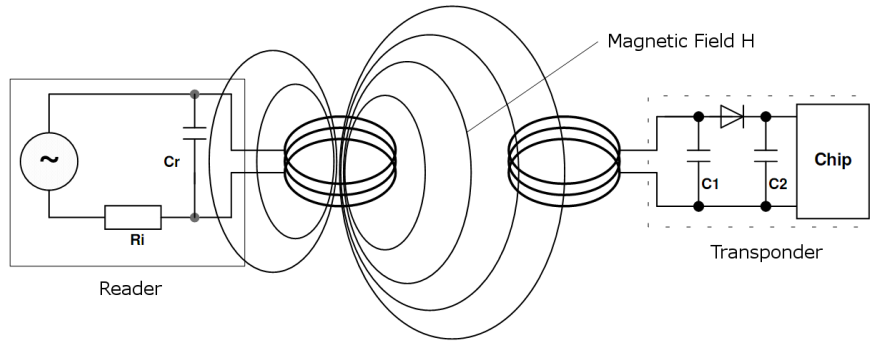
Figure 2.9.: Working Principle for a Passive Transponder [Fin06, page 42]

transponders is therefore contradictory. As the coupling in air is naturally very weak, the effect of resonance is used to increase the operating distance.

2.3.2. Parallel Resonance

The RFID chip, the capacitor and the antenna coil form a parallel resonance circuit. Figure 2.10 shows the equivalent circuit model for the coil and the chip. The coil is modelled as an inductor L with the series resistance R_L and a parasitic capacitance C with a loss conductance value G_C. C_1 is the tuning capacitance, used to tune the resonance frequency to the operating frequency of 13.56 MHz. C_2 and R are the RFID chip internal resistance and capacitance. Modelling the RFID chip as a capacitor and a resistor is just an approximation which holds as long as the chip is not operating. For a precise model, the chip needs to be modeled in more detail. For now the model is assumed to be accurate enough. Summing up the parallel capacitors and the parallel resistances leads to a simple lossy parallel resonant circuit.
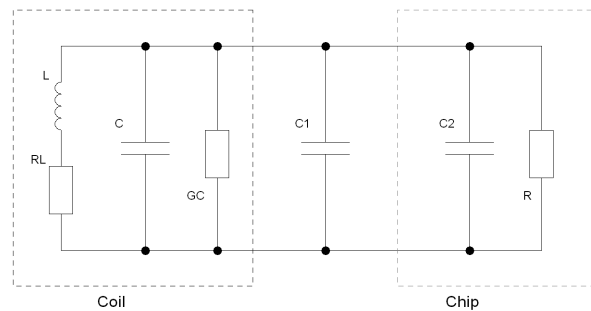
Figure 2.10.: Equivalent Circuit for the RFID System

The resonance frequency for the resonance circuit shown in figure 2.11 is given by:

$$\omega_r = \sqrt{\frac{L - R_L^2 C_t}{L^2 C_t}} \tag{2.1}$$
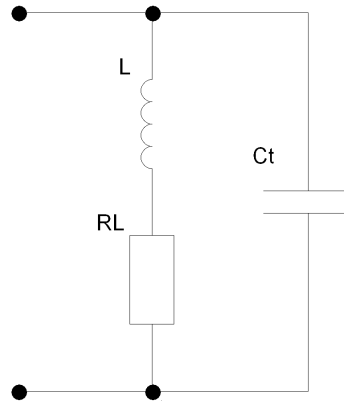
Figure 2.11.: Equivalent Resonance Circuit

Where L is the inductance of the antenna coil, R_L is the series resistance of the antenna coil and C_t is the total parallel capacitance.

2.4. Design and Characterization of Planar Coils

As mentioned in the previous section, the resonance frequency of the system is important for a proper operation of the RFID application. The resonance frequency (see equation 2.1 on the preceding page) is a function of the coil inductance, the coil capacitance, the coil resistance and the additional capacitances added in form of a tuning capacitance or a chip input capacitance. To design an optimal system, all these parameters need to be known. Hence, the producer of the coil needs to know the precise inductance, resistance and capacitance of his coil. The calculation of this characteristic parameters can be done by using empirical formulas or simulation programs. Various empirical formulas exist for the calculation of the inductors of planar coils ([NJS+97], [AB03], [Leo03], [Lee03] or [MdMHBL99]). The disadvantage of these formulas is that they mostly neglect high frequency effects like eddy currents and the skin effect in the conductor and they all assume a special geometry and are only valid for this geometry. Additionally the conductor material is assumed to be a non magnetic material. As soon as magnetic materials are brought close to the coils or included in the coil design, a different way of calculating the coil impedance is necessary. The parasitic capacitance calculations are mostly based on planar coils, manufactured on chip and therefore based on a silicon substrate. In this case, the coil is based on a non conducting glass substrate. To overcome these limitations, this thesis deals with the characterization of the coils via electromagnetic field simulation.

In this chapter it was shown that the exact knowledge of the coil properties is essential. In the following chapter the experimental characterization of the present coils and the most important material parameters is presented.

3. Experimental Characterization

In this chapter the existing coil geometry and the materials used are characterized by various experimental techniques. The parameters of interest are the coil inductance, the coil resistance and the coil self capacitance. The most important unknown material parameters are the relative permeability and the volume resistivity of the electroplated nickel used for the conductor material.

3.1. Coil Impedance Measurement

Assuming the coil equivalent circuit shown in figure 2.10 on page 23, the parameters of interest are the coil inductance L, the coil resistance R_L and the coil capacitance C.

3.1.1. Measurement Technique

Measurement Device

The impedance measurements were carried out using the vector network analyzer Bode 100 from Omicron Lab [Lab09].

3-Point Calibration

3-point calibration was used for all the measurements carried out during this work. By measuring three known impedance values, the influence of the connection setup and probing system on the measurement can be removed. The three used calibration points are "open" ($Z = \infty$), "short" ($Z = 0$) and "load". To realize the "load" point a known ohmic resistor is connected to the system. For that a resistor with low parasitic inductance respectively capacitance has to be used. In this case two $100\,\Omega$ SMD[1]-resistors were connected in parallel to realize a $50\,\Omega$ resistor for load calibration. For high precision measurements at higher frequencies a special high frequency resistor should be used.

---
[1]Surface Mounted Device

Probe and Connection Setup

For repeatable results and simple calibration a prober system is essential. Due to lack of a prober station, a special probing system was designed and built. The used probing needles have a spring to guarantee constant probing force and are gold plated to ensure low contact resistance. The first probe system was an unbalanced probe. Meaning the measurement current flows through the shield of the coax cable. The disadvantage of this probing system could be seen when rotating the DUT[2] about 180°. [SSC08] presents a balanced probe for impedance measurements. A similarly connection setup was used for the impedance measurements (see figure 3.1). Figure 3.2 on the next page shows the difference in results for the balanced and unbalanced probing. The DUT rotation has less influence on the results gathered with the balanced probing system. Therefore the balanced probe was used to carry out the impedance measurements. Figure B.2 and B.1 in appendix B show that the balanced probe also improves the resistance measurement results.

(a) Unbalanced Setup   (b) Balanced Setup
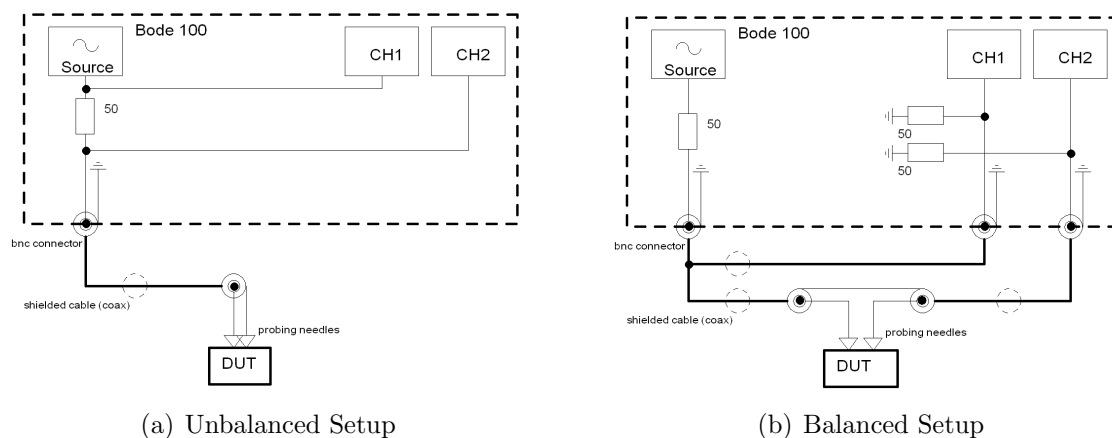
Figure 3.1.: Measurement Connection Setup

To reach repeatable results probing needles with springs were used. The advantage is the repeatable contact pressure and the low contact resistance due to the gold plated surface. Due to the existence of a spring in the probes, the results have to be checked especially in the high frequency range. During the measurements carried out in this work, no problems occurred by the use of the probe needles. Figure 3.3 on page 28 displays the used probe configuration for the impedance measurements. The probing needles produce a contact pressure of $3\,\mathrm{N}$ and therefore guarantee a low contact resistance.

---

[2]Device Under Test
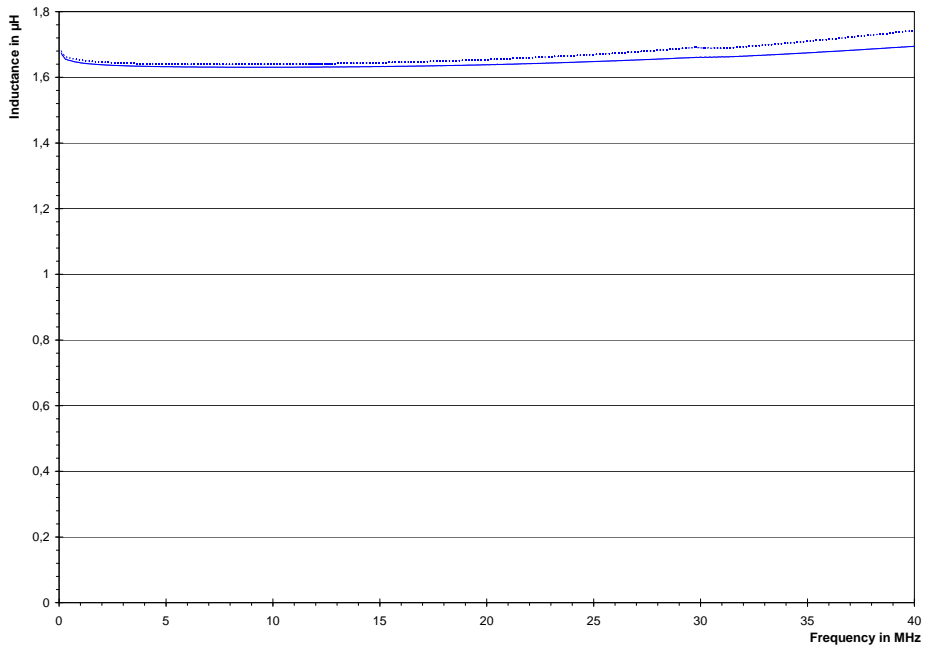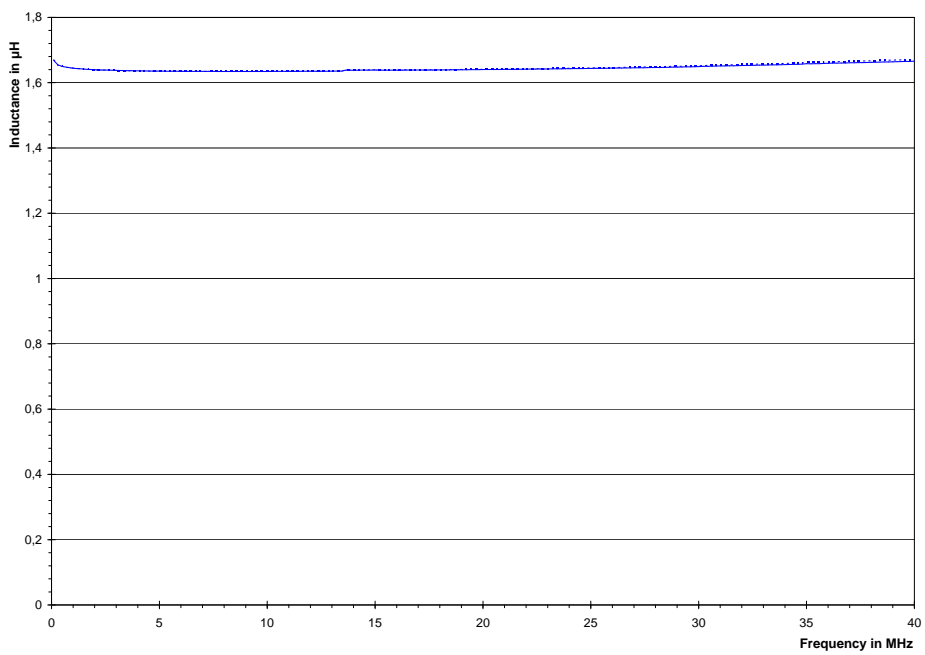
(a) Unbalanced Probe

(b) Balanced Probe

Figure 3.2.: Inductance Measurement (Solid line . . . device under test not rotated, dotted line. . . device under test rotated about 180°)

27
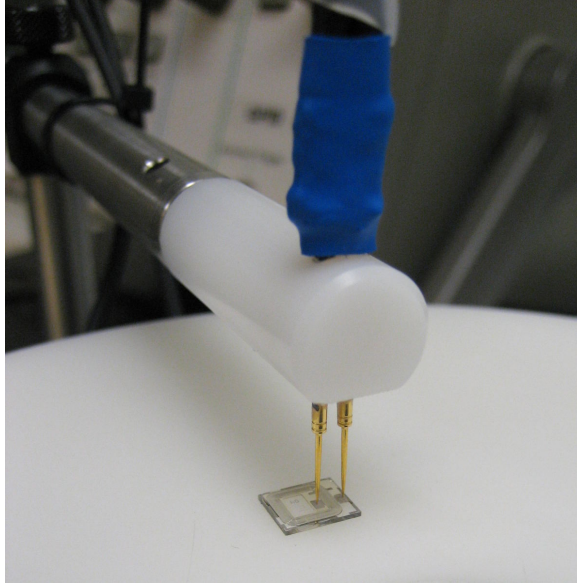
Figure 3.3.: Probe Configuration for Coil Impedance Measurement

3.1.2. Measurement Results

The following measurement results were gathered using the probe setup presented in the previous part (see figure 3.3). Measurements were carried out on isolated coils from a single wafer (internal wafer number: 080110-02). Figure 3.4 on the facing page shows the measured impedance (resistance and inductance values) in a frequency range from $10\,\text{kHz}$ to $40\,\text{MHz}$. At $13.56\,\text{MHz}$ the average measured inductance is $(1.634 \pm 0.021)\,\mu\text{H}$ and the average resistance value is $(19.12 \pm 1.66)\,\Omega$. The error calculation can be found in appendix C.3 on page 92. Table 3.1 on page 30 summarizes the measured results:

3.1.3. Measurement Validation

To verify the measurement technique, a coil was measured by the EMT[3] department at the Graz University of Technology (http://www.emt.tugraz.at/. The results achieved by the EMT department are:

$$L = 1.630\,33\,\mu\text{H}, \qquad R_L = 20.0096\,\Omega$$

Comparing the EMT results with the measurement results presented in table 3.1 on page 30. The resistance values differ about $4.5\,\%$ and the inductance values differ about $0.2\,\%$.

---

[3]Institute of Electrical Measurement and Measurement Signal Processing
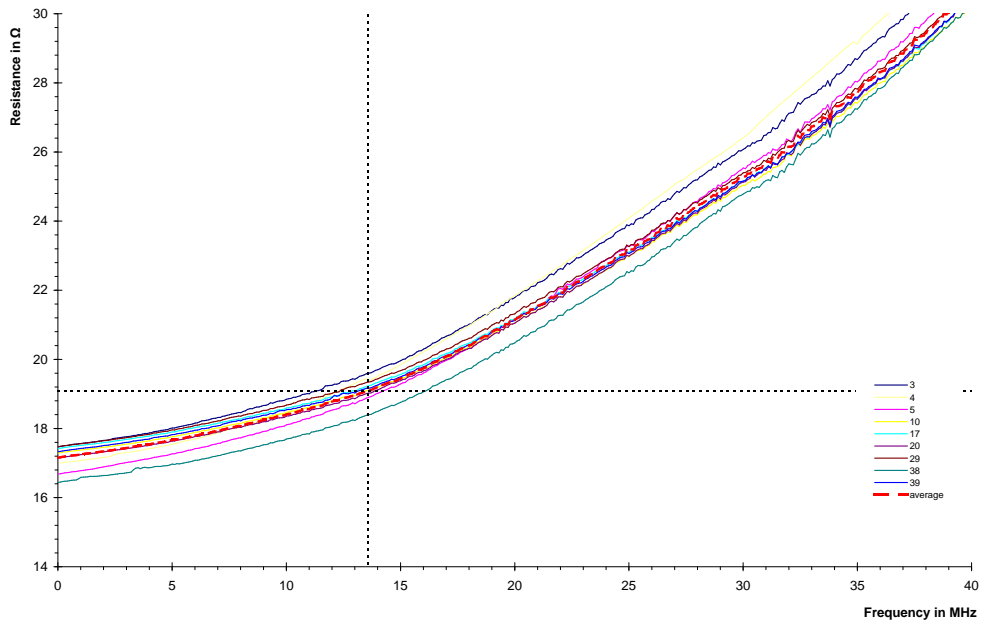
(a) Resistance Measurement
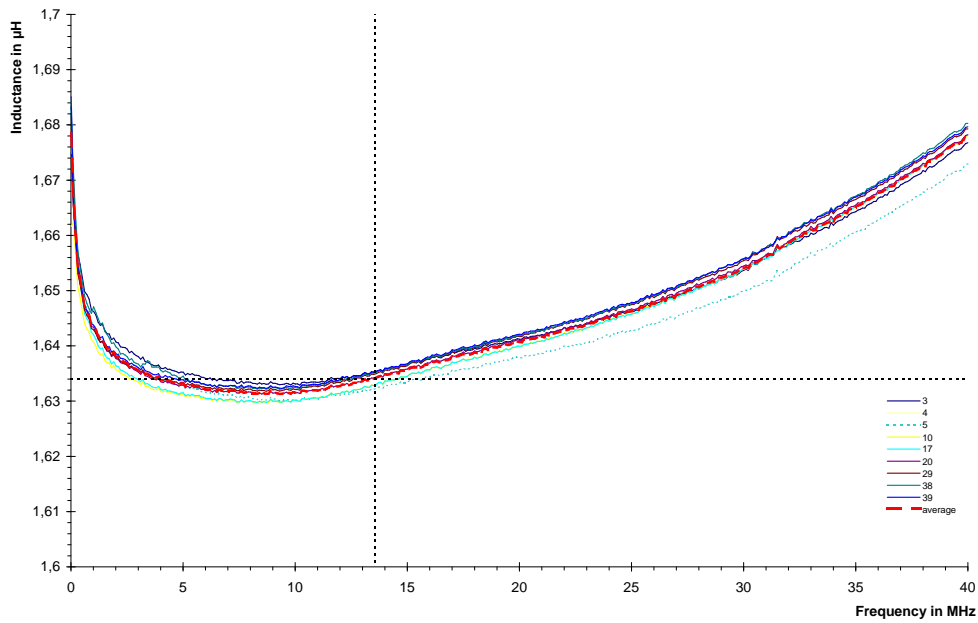
(b) Inductance Measurement

Figure 3.4.: Measurement results for isolated coils. The series names equal the on-wafer coil numbers. Internal wafer number: 080110-02

3. Experimental Characterization

Table 3.1.: Measured impedance values at 13.56 MHz

Coil No.	R_s	L
-	Ω	μH
03	19.59	1.635
04	19.41	1.637
05	18.89	1.632
10	19.10	1.633
17	19.23	1.633
20	19.02	1.635
29	19.34	1.635
38	18.39	1.635
39	19.17	1.634
average	**19.12**	**1.634**
std. dev	0.35	0.0015

3.2. Geometrical Deviations

In the beginning, the design of the available coil geometry was presented. In reality the fabricated geometry slightly differs from the design. The reason for this are the fabrication processes which don't produce "ideal" geometrical forms.

To investigate the most important deviations, a processed planar coil was cut in half. After embedding in a polymer, grinding and polishing the geometry can be directly viewed with an optical microscope.
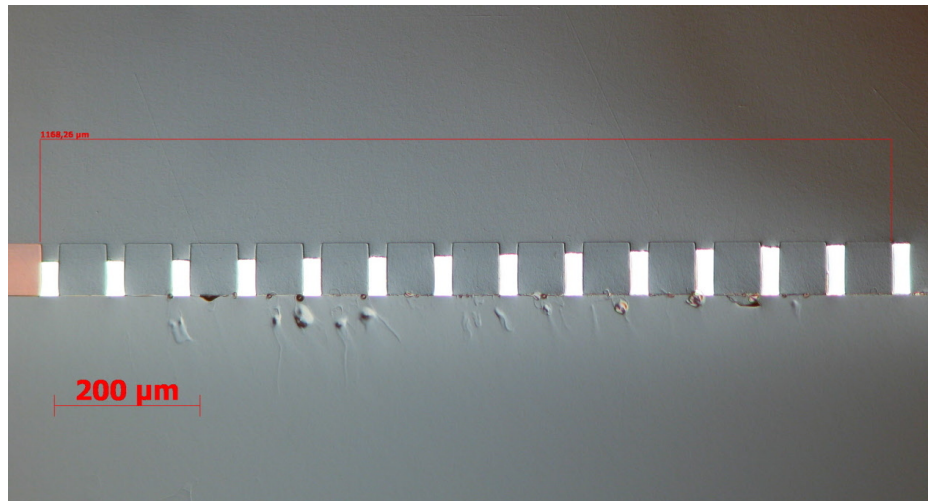
Figure 3.5.: Coil cross section through the 14 windings

Figure 3.5 depicts the 14 windings of the coil. The left side is the inner winding and the right side the outer winding. The height of the conducting material (bright zones)
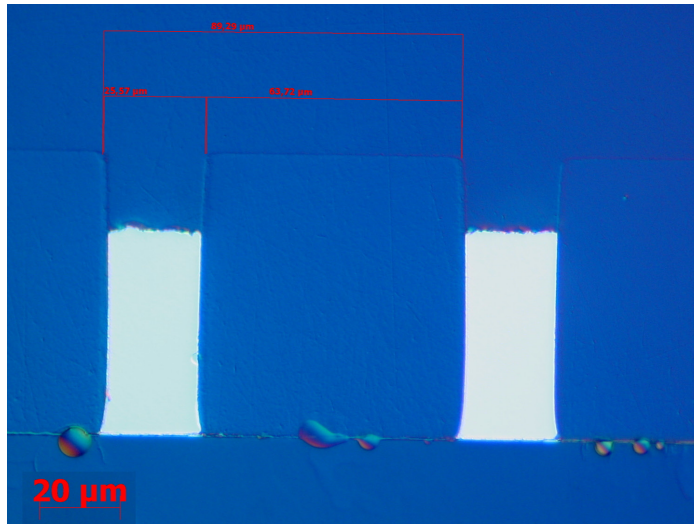
Figure 3.6.: Conductor cross section detail

is not constant over the cross section. The reason for that is the electroplating process. Due to the fact, that the seed layer is structured before the electroplating, points on the inner windings have a higher resistance to the electroplating current source than points on the outer windings.

Figure 3.6 shows the cross sectional form of the conductors in detail. In theory the cross section of the conductor should form a rectangle with dimensions of $30\,\mu\text{m} \times 100\,\mu\text{m}$. In reality, the side edges are not straight and the width of the conducting material is lower than $30\,\mu\text{m}$.

3.3. Material Characterization

The planar coil consists of multiple materials. These are:

- Pyrex (substrate)
- SU-8 (photoresist)
- Nickel (electroplated wire)
- Titanium (seed layer)
- Copper (seed layer)

The physical properties affecting the electrical properties of the coil are the electric resistivity ϱ in $\Omega\,\text{m}$, the magnetic relative permeability μ_r, the relative permittivity ϵ_r and the loss tangent $\tan\delta$. Whereas the resistivity of copper and titanium is known, the resistivity of the electroplated nickel is unknown. Like the resistivity, the permeability of the electroplated nickel is not known. A value for the SU-8 permittivity

is provided by the material supplier, however the influence of the nickel electroplating on the SU-8 permittivity is unknown. In the following, the material parameters, having the greatest influence on the simulation results are identified via experimental measurements.

3.3.1. Nickel Permeability

The relative permeability μ_r has a strong influence on the simulation results. In literature, values from 20 to 1500 are given (see [OWK+09] or the MatWeb website). The present coil is produced by using a special nickel electroplating process. The process parameters can be found in appendix A. For this specific process, no values for the relative permeability can be found. Therefore, the electroplated nickel produced with the process parameter from table A.2 on page 87 has to be characterized.

Characterization via Coil Inductance Measurement

The permeability of the electroplated nickel can be measured by coil inductance measurement. The inductance L of a toroidal coil according to [KMR08, equation 23.8] is given by

$$L = N^2 \frac{\mu b}{2\pi} \ln \frac{r_2}{r_1} \tag{3.1}$$

Where N is the number of windings, μ the permeability of the core material, b the thickness of the coil and r_1 and r_2 are the inner and outer radius of the toroid.

From equation 3.1 we see that the inductance L is a function of geometry and permeability of the core material. As the geometry is known and the inductance can be measured, the permeability of the core material can be identified. For experimental results the following coils were produced:

1. Toroidal air coil (see figure 3.7 on the facing page)

2. Toroidal coil with single layer nickel core (see figure 3.8 on the next page)

3. Toroidal coil with laminated nickel core (see figure 3.9 on the facing page)

The toroidal air coil has a non magnetic core (plastics) and is used to verify the experimental technique. For the other coils, two nickel layers were produced by electroplating using the process parameters from table A.2 on page 87. The first layer has a thickness of approximately 490 µm and the second layer has a thickness of approximately 45 µm. The first layer was cut into a toroidal form using conventional milling technique. From the second nickel layer 11 toroids were cut using femto-second laser cutting. Using these 11 toroids, a laminated core where the single layers are electrically isolated from
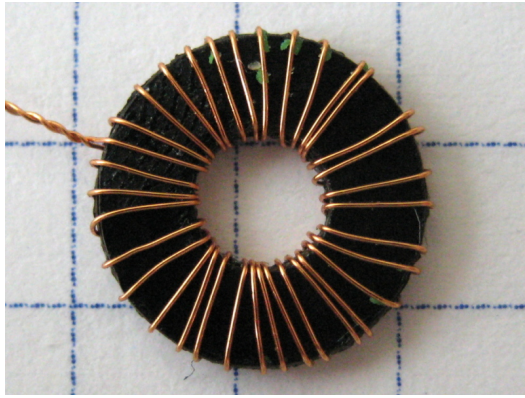
(a) Aircoil

(b) Core detail

Figure 3.7.: Coil No. 1: Toroidal coil with plastics core
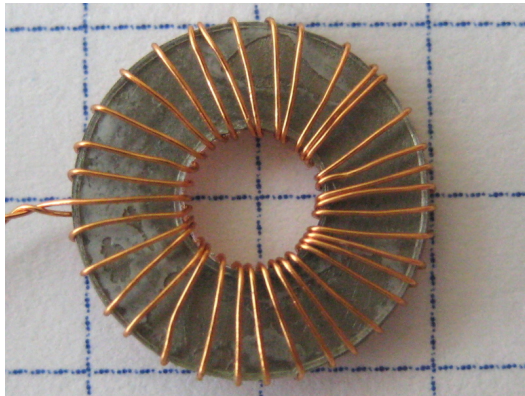
(a) Nickel core
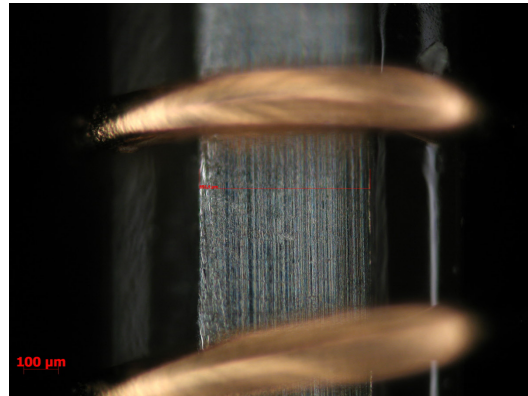
(b) Core detail

Figure 3.8.: Coil No. 2: Toroidal coil with single layer nickel core
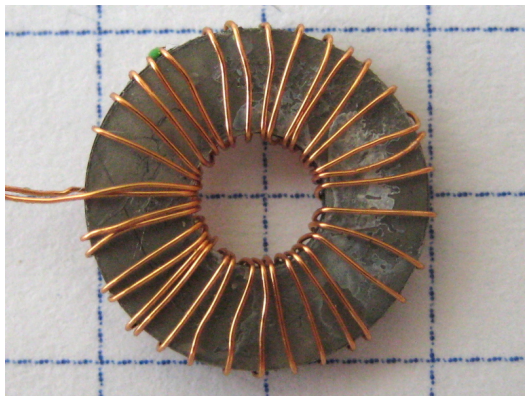
(a) Laminated nickel core

(b) Core detail

Figure 3.9.: Coil No. 3: Toroidal coil with multilayer nickel core

each other was produced. This results in reduction of eddy currents in the core and therefore increases the maximum operation frequency of the coil.

The geometrical properties of the coils are shown in the following table. r_1 is the inner radius of the toroidal coil, r_2 the outer radius of the toroidal coil, b is the thickness or height of the toroid, N the number of windings and A_{ni} is the cross sectional area of the nickel containing part of the core.

Table 3.2.: Geometrical properties of toroidal coils

Coil No.	r_1	r_2	b	N	A_{ni}
-	mm	mm	mm	-	mm^2
1	1.92	5.12	1.25	34	0
2	1.85	5.14	1.27	35	1.473
3	1.84	5.16	1.37	35	1.534

Impedance Measurement

The Impedance of the coils was measured using the BODE100 vector network analyzer in the frequency sweep mode. The measurement cable was compensated using 3 point calibration (open, short and $50\,\Omega$). The results are shown in figure 3.10, 3.11 and 3.12 on the facing page.

The measurement frequency range was chosen from $100\,\mathrm{Hz}$ to $10\,\mathrm{kHz}$. The inductance and the resistance values of the air coil are constant over the whole frequency range (see figure 3.10 on the next page. The inductance and resistance values of the single layer nickel core vary with frequency which can be seen in figure 3.11 on the facing page. The reason for this are most likely eddy currents in the core material. Using a laminated core where the single nickel layers are electrically insulated from each other, reduces this effect (see figure 3.12 on the next page. Table 3.3 on page 36 summarizes the results of the measurements. The aircoil has an inductance of $0.337\,\mathrm{\mu H}$. The single layer core coil has an inductance of $1.609\,\mathrm{\mu H}$. The laminated core coil has an inductance value of $1.667\,\mathrm{\mu H}$.

Permeability Calculation

Reordering of equation 3.1 on page 32 leads to:

$$\mu_r = \frac{L2\pi}{N^2 \mu_0 b \ln \frac{r_2}{r_1}} \tag{3.2}$$

Using the geometric values from table 3.2 and the measured inductance values from table 3.3 on page 36 the average relative permeability of the core material can be
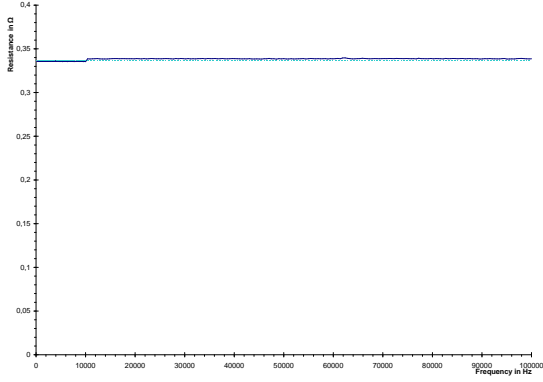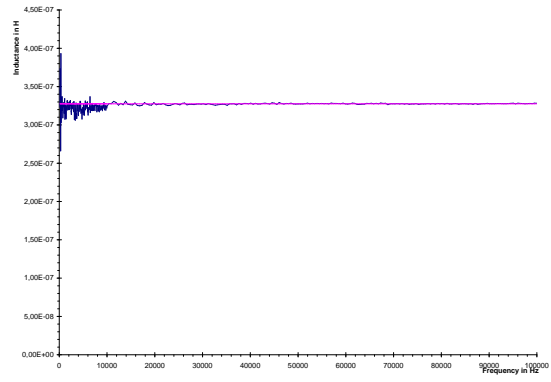
(a) Coil resistance

(b) Coil inductance

Figure 3.10.: Measurement results for Coil No. 1, air core
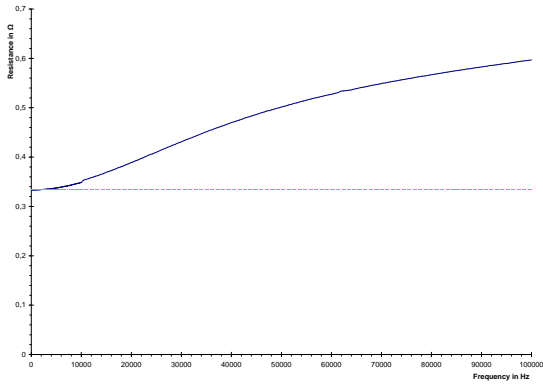
(a) Coil resistance
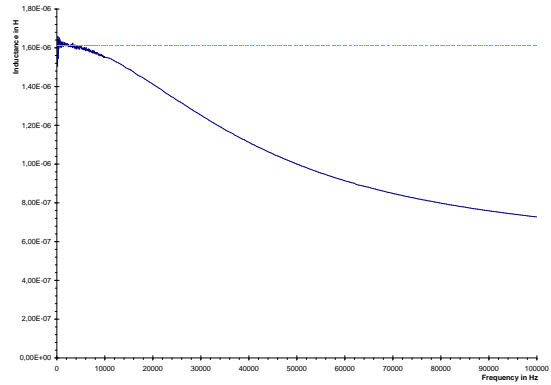
(b) Coil inductance

Figure 3.11.: Measurement results for Coil No. 2, single layer nickel core
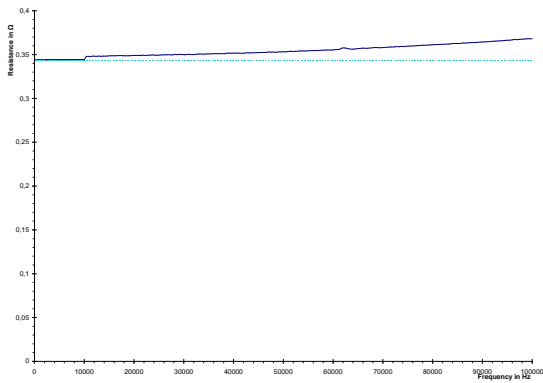
(a) Coil resistance
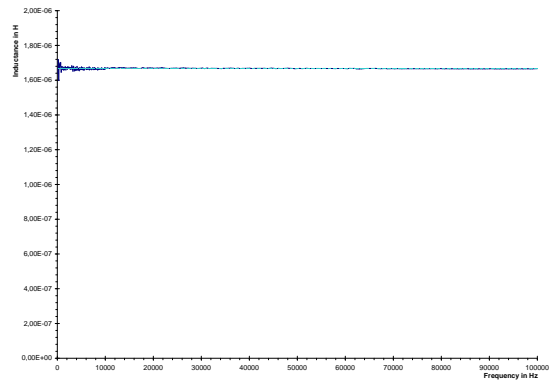
(b) Coil inductance

Figure 3.12.: Measurement results for Coil No. 3, laminated nickel core

35

Table 3.3.: Impedance and Average Relative Permeability

Coil No.	L	$\bar{\mu}_r$
-	μH	-
1	0.337	1.028
2	1.609	5.053
3	1.667	4.805

calculated. The following table shows that the relative permeability calculated for the air coil is 1.028, which nearly matches the expected value of 1.

The calculated average relative permeability for the coils with nickel core is 5.053 for the single layer coil and 4.805 for the laminated core coil. To reach the relative permeability of the nickel, the amount of nickel in the core has to be considered. The magnetic permeance Λ analog to the electrical conductivity is defined as:

$$\Lambda = \frac{1}{R_m} = \frac{\mu_0 \mu_r A}{l_m} \tag{3.3}$$

Where R_m is the magnetic resistance, μ_0 the permeability of free space, μ_r the relative permeability, A the cross sectional area and l_m the circuit length.

The cross section of the toroidal core contains plastics material ($\mu_r = 1$) and nickel ($\mu_r = ?$) The magnetic permeance for each part is given by:

$$\bar{\Lambda} = \frac{\mu_0 \bar{\mu} \bar{A}}{l_m} \tag{3.4}$$

$$\Lambda_{ni} = \frac{\mu_0 \mu_r A_{ni}}{l_m} \tag{3.5}$$

$$\Lambda_p = \frac{\mu_0 A_p}{l_m} \tag{3.6}$$

Where $\bar{\Lambda}$ is the total permeance of the core, Λ_{ni} is the permeance of the nickel containing part of the core and Λ_p is the plastic containing part of the core. $\bar{A}$ is the total cross sectional area of the core, A_{ni} is the cross sectional area of the nickel containing part, and A_p is the cross sectional area of the plastics containing part. l_m is the length of the circuit which is approximately the same for all parts because the material practical only differs in z-direction.

Connecting the plastic and nickel containing parts in parallel, leads to the total core. This can be expressed as the sum of the magnetic permeance:

$$\bar{\Lambda} = \Lambda_p + \Lambda_{ni} \tag{3.7}$$

Inserting equation 3.4 and reordering leads to:

$$\mu_r = \frac{\bar{\mu}\bar{A} - A_p}{A_{ni}} \tag{3.8}$$

Using the previous result and the geometrical values for the core from table 3.2 on page 34 the relative permeability of the nickel is calculated. This results in $\mu_r = 12,5$ for coil no. 2 and $\mu_r = 12,3$ for coil no. 3.

The average of these two results and the from now on assumed value for the permeability of the specific nickel layer is:

$$\underline{\mu_r = 12.4} \tag{3.9}$$

The worst case error is $8.7\,\%$. The error estimation can be found in appendix C.1 on page 91

3.3.2. Nickel Resistivity

Additionally to the permeability the resistivity of the electroplated nickel is of interest. By cutting a $50\,\mu\text{m}$ thick nickel foil with a femto-second laser, a wire with a length of $758.6\,\text{mm}$ was fabricated. Through measuring the geometry of the wire and the DC-resistance, the resistivity of the material can be identified. The resistance of a wire is given by:

$$R = \varrho \frac{l}{A_{ni}} \tag{3.10}$$

where R is the resistance value, l the length of the wire and A_{ni} the cross sectional area of the wire. Laser cutting leads to an approximately trapezoidal cross section (see figure 3.13). The measured geometrical values are presented in table 3.4 on the next page.
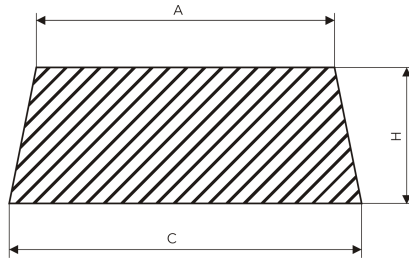
Figure 3.13.: Approximate Cross Section of the Nickel Wire

The measured DC-resistance is $R = 6.09\,\Omega$. Using equation 3.10 with the measured resistance and the geometrical values from table 3.4 the resistivity ϱ can be calculated. The resulting resistivity is

$$\underline{\varrho = 8.64 \times 10^{-8}\,\Omega\,\text{m}} \tag{3.11}$$

with a maximum possible error of $7\,\%$ (see appendix C.2 on page 91).

Table 3.4.: Measured Geometry Values

Parameter	Value
-	µm
A	224.6
H	46.5
C	238.5
l	758567

3.4. Summary

An experimental setup for the coil impedance measurement is presented. The measured results are verified by comparing results with results from the EMT institute at the Graz University of Technology. The coil inductance at 13.56 MHz was found to be $L = 1.634\,\mu\text{H}$ and the coil resistance $R_L = 19.12\,\Omega$.

The material characterization shows that the relative permeability of the electroplated nickel is much lower than values from literature. A value of $\mu_r = 12, 4$ has been measured. As the permeability values in literature reach from 20 to 1500, this is an interesting result. The electroplated nickel has a much lower permeability than bulk nickel. The resistivity is higher than for bulk nickel. A resistivity of $\varrho = 8.64\,\Omega\,\text{m}$ has been measured. In addition, the investigation of the change of the material properties with respect to variation of process parameters would be of interest.

4. Simulation Method

In the following chapter the coil geometry is characterized using an electromagnetic finite element simulation technique. For further details on the finite element technique on electromagnetic fields, the interested reader is refered to literature like [KMR08], [BLT93] or [Jac98].

The simulations in this chapter are carried out as three dimensional and two dimensional magnetic and electric field calculations. The results are compared with results derived from the Institute for Fundamentals and Theory in Electrical Engineering at the Graz University of Technology (http://www.igte.tugraz.at/).

4.1. Calculation Objective

The parameters of interest are the lumped equivalent circuit parameters, namely

- R_L as the series resistance of the coil,

- L as the inductance of the coil and

- C the self capacitance of the coil geometry.

The coil is assumed to behave like a parallel resonance circuit. The equivalent circuit model is shown in figure 4.1.
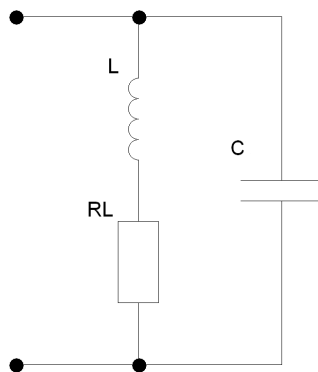
Figure 4.1.: Coil equivalent circuit model

4.2. Simulation Approach

The Research Centre for Microtechnology uses the finite element simulation program ANSYS®Academic Research, v.12.0. The program offers various element types applicable for electromagnetic field calculations which implement different approaches. The available possibilities are

- Electric flow field

- Static magnetic and electric fields

- Quasi static magnetic field including eddy currents

- Quasi static electric field

- High frequency "full wave" electromagnetic field

The mentioned calculation objectives can be derived in different ways. Solving the full set of maxwell equation by doing a "full wave" electromagnetic field simulation would deliver all results in one simulation. The computational effort for this calculation would be very high. A possibility to overcome this problem is to calculate the quasi static magnetic and the quasi static electric field separately. This means that the coupling between the magnetic and electric field is neglected and therefore no wave propagation is calculated. As long as the structural size of the calculated geometry is much smaller than the wave length of the electromagnetic field, this approximation holds. At $13.56\,\mathrm{MHz}$ the related wavelength is $\lambda = \frac{c}{f} \approx 22\,\mathrm{m}$. The maximum structural size of the geometry is the length of the coil wire. With a wire length of $0.252\,\mathrm{m}$, the geometrical size is about 100 times smaller than the wavelength. Therefore the quasi static approximation holds for this problem.

In [BBM+05] an approach for the FEM modelling of micro coils is presented. For this work a similar approach is chosen. The following enumeration lists the two main steps of this approach:

1. Simulation of the quasi stationary magnetic field to derive the coil inductance L and the coil resistance R_L considering eddy currents.

2. For the calculation of the coil self capacitance C, a separate static electric field analysis is carried out.

4.3. 3D Magnetic Field Simulation

4.3.1. Geometry and Simplifications

The geometry of the coil is shown in figure 4.2 on the next page. The substrate material carries the electroplated conductors and the photoresist which works as an

insulation between the single windings. The coil winding starts and ends at the chip-respectively capacitor connection pads.
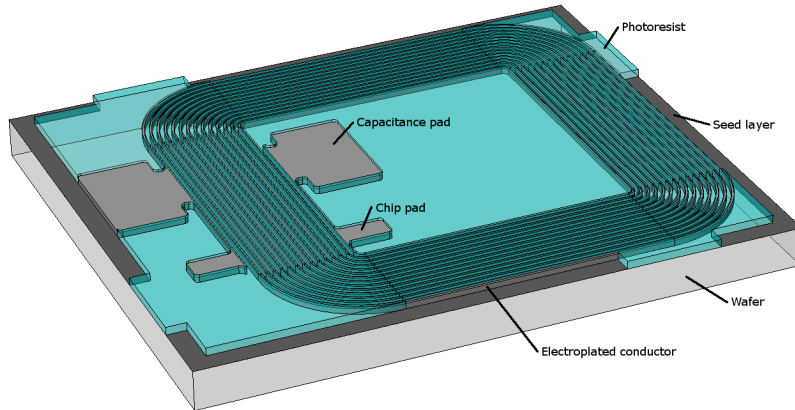
Figure 4.2.: Coil geometry

The inductance is mainly dependent on the geometrical form of the coil windings which restrict the main current flow path. Therefore the geometry of the pads is negligible. Neglecting the capacitance pads, the chip pads and the 300 nm thick seed layer areas leads to the simple coil geometry illustrated in figure 4.3(a). This geometry shows a symmetry in the magnetic field which leads to the quarter model, presented in figure 4.3(b).
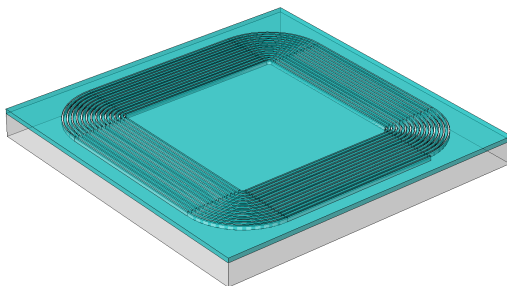
(a) Simplified full model
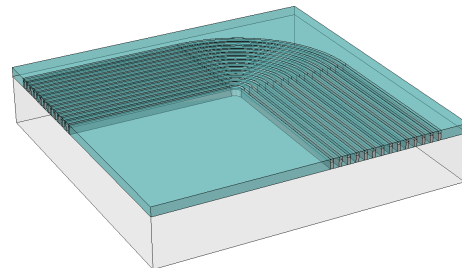
(b) Quarter model

Figure 4.3.: Geometrical simplification and symmetry

4.3.2. Analysis and Element Types

As eddy currents shall be considered in the simulation, a time dependent analysis has to be performed. Assuming sinusoidal currents and linear material behaviour leads to a harmonic analysis type. Ansys supports the three dimensional harmonic simulation of magnetic fields with various element types. Two main types of elements are applicable for the 3D magnetic harmonic analysis.

4. Simulation Method

- Node based magnetic vector potential

- Edge based magnetic vector potential

According to [Inc09, Theory Reference] the node based vector potential formulation is not correct for models containing materials with different permeabilities. The conductor in this case is made of nickel with a relative permeability greater one. Hence the only applicable elements are the edge based elements. The Ansys release 12.0 supplies two types of 3D-magnetic edge elements.

1. Solid 117

2. Solid 236,237

In the following these element types are explained in detail.

Solid 117 Element

The solid 117 element is a 20 node element with 12 edge flux DOF[1]s, one at each mid side edge node. (Ansys specific label: **AZ**). The eight corner nodes carry the DOF **VOLT**. That is either the time integrated electric potential when using the *classical formulation* or the electric potential when using the *solenoidal* formulation. To consider eddy currents in the current conducting regions, the classical formulation has to be used.
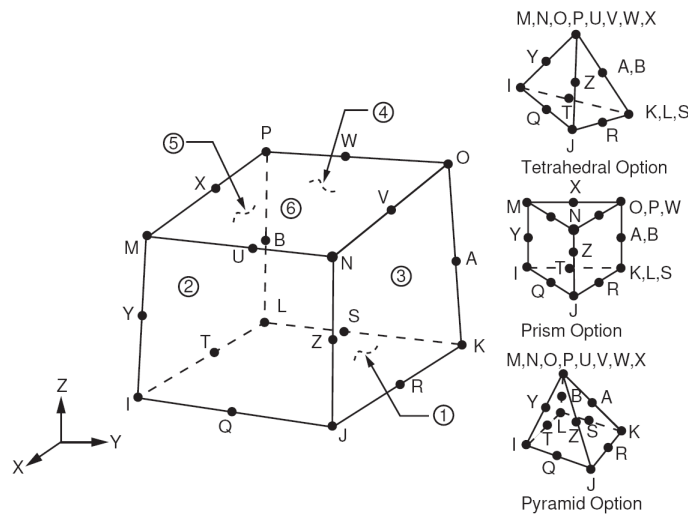
Figure 4.4.: Solid 117 Geometry [Inc09, Element Reference]

The solid 117 element models quasi static magnetic fields including eddy current effects but neglects the displacement current (electric flux density).

---

[1]Degree Of Freedom

42

Solid 236,237 Element

The solid 236 and 237 electromagnetic elements are available since the ANSYS release 12.0 (May/June 2009). As this is a new element type, not all features are documented yet. The reason why it is presented here, is the fact that it can be used similar to solid 117 but it is numerically more stable. The better quality of the results can be recognized at simulation results in section 5.2 on page 68.

(a) Solid 236   (b) Solid 237
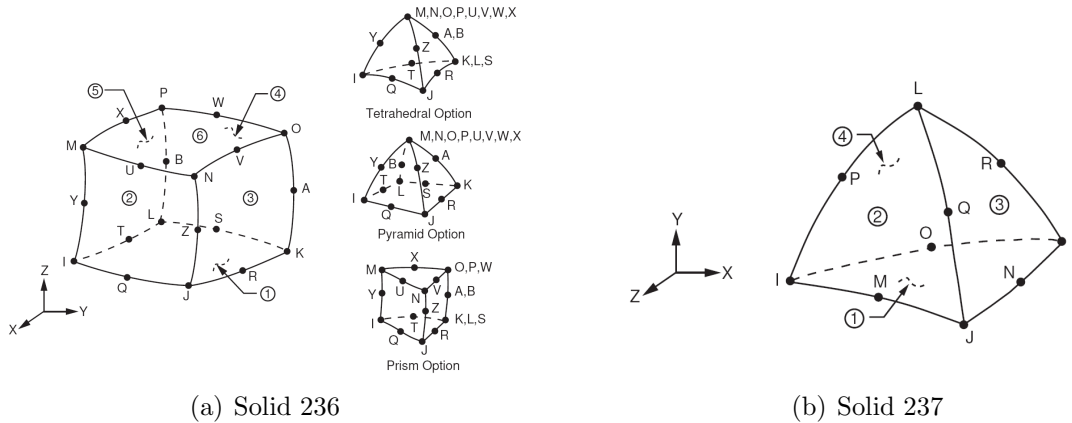
Figure 4.5.: 236,237 element geometry [Inc09, Element Reference]

Additionally the element has two geometrical shapes. Hexahedral shape with 20 nodes and tetrahedral shape with 10 nodes. Using the tetrahedral element with 10 nodes instead of the degenerated hexahedral element with 20 nodes, reduces the DOF number and therefore reduces calculation time.

The 3D magnetic harmonic simulations presented in this section are performed using the solid 117 element.

Harmonic Analysis

As mentioned before, the analysis is a time dependent analysis. Therefore a calculated field quantity q is dependent on the time t and the space vector r. In a harmonic analysis, the quantities are chosen to be periodic functions like

$$q(r, t) = a(r) \cos(\omega t + \Phi(r)) \tag{4.1}$$

respectively

$$q(r, t) = c(r) \cos(\omega t) + s(r) \sin(\omega t) \tag{4.2}$$

where r is the location vector in space, t the time, ω the angular frequency, $a(r)$ the amplitude, $\Phi(r)$ the phase angle, $c(r)$ the measurable field at $\omega t = 0°$ and $s(r)$

the measurable field at $\omega t = -90°$. More details can be found in [Inc09, Theory Reference].

This "complex formulation" reduces the problem to a problem dependent on space but not on time. $c(r)$ is the real part and $s(r)$ the imaginary part of the complex quantity $Q(r)$. According to this, every quantity in a harmonic analysis has a real and an imaginary part.

$$Q(r) = Q_r(r) + jQ_i(r) \tag{4.3}$$

4.3.3. Materials

The model contains the following physical materials:

- Air

- Pyrex (substrate material)

- Nickel (conductor material)

- SU-8 (photoresist)

Whereas the physical properties of air and Pyrex are well known, the properties of SU-8 and especially the nickel are unknown. Section 3.3 deals with the characterization of the materials. For the magnetic field calculation the relative permeability μ_r (Ansys label **MURX**) of the material and the resistivity ϱ (Ansys label **RSVX**) of the material has to be known. In the following table the material parameters used for the 3D magnetic field simulation are shown.

Table 4.1.: Magnetic material parameters

Material	μ_r	ϱ
-	1	$\Omega\,\mathrm{m}$
Air	1	-
Pyrex	1	-
SU-8	1	-
Nickel	1240	6.4×10^{-8}

As already mentioned above, the nickel wires are the only magnetic materials in the model. As the permeability and resistivity of the electroplated nickel were not known before the characterization, the values from the MatWeb website `http://www.matweb.com` are used in the following calculations.

4.3.4. Mesh

To obtain exact results, a proper mesh has to be generated. In the case of using Ansys with the solid 117 element, the following points, regarding the mesh have to be considered:

- At least 3 to 5 elements should resolve the skin depth area in the conductor.

- For the current carrying regions hexahedral elements should be used for accurate results.

- The minimum allowed edge length is 1×10^{-6}.

- As no infinite boundary elements are available, as much air as possible should be modelled.

(a) Geometry

(b) Air mesh

(c) Mesh detail

(d) Conductor swept mesh
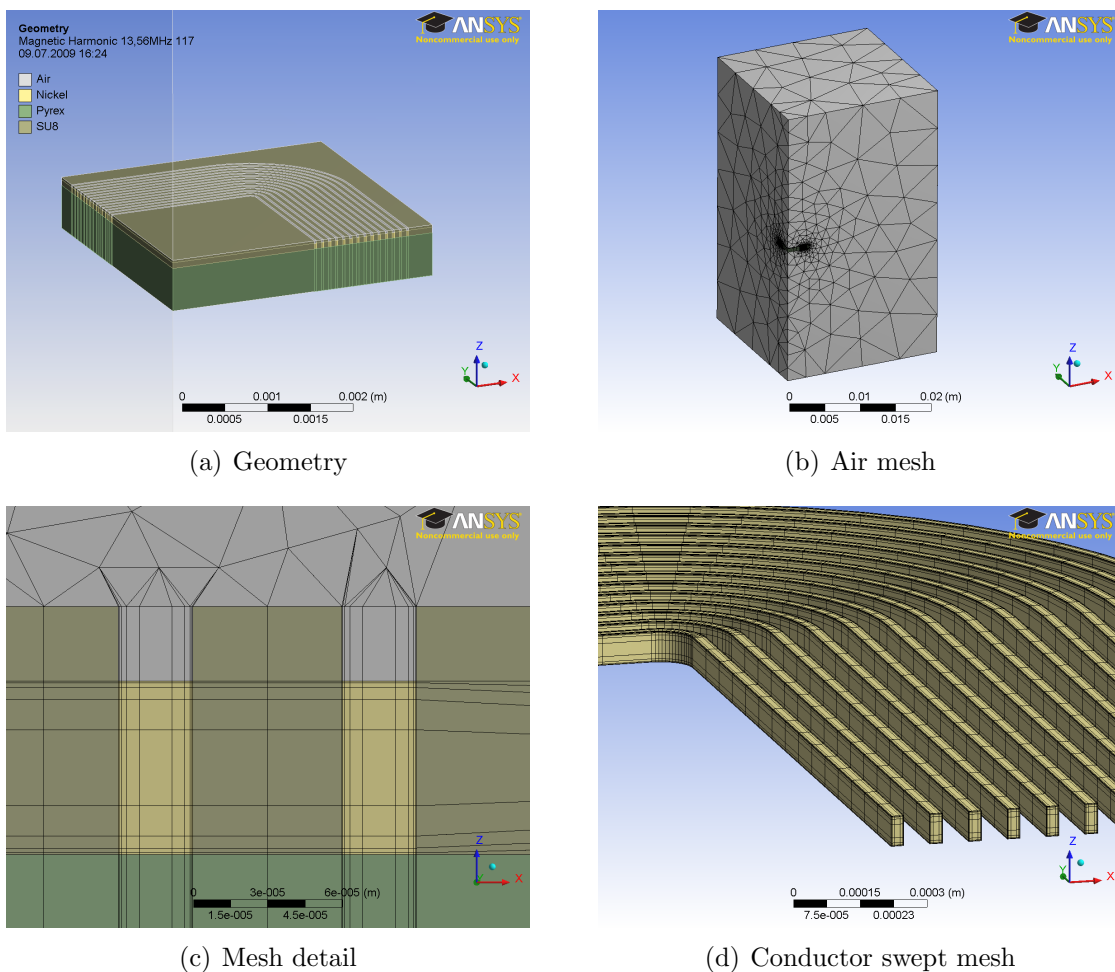
Figure 4.6.: Mesh and geometry

Considering the points from above, a mesh like shown in figure 4.6(b) can be generated by using available sizing controls. The geometry and mesh were generated in Ansys

Workbench Release 12.0. Figure 4.6(a) shows the modeled geometry and figure 4.6(b) depicts the mesh including the meshed air. The size of the air, surrounding the coil is approximately 20 mm at each point from the geometry. Figure 4.6(c) shows the mesh in detail. The color of the mesh indicates the material assigned with the mesh. The conductors are meshed with hexahedrons (see figure 4.6(d)). The edge length of the elements decreases at the conductor surface. The reason for this is that the current density variation is high at the conductor surface due to the skin effect. The element edge length parallel to the direction of the current flow is large compared to the element edge length perpendicular to the current flow. This reduces the total number of elements in the model. It is allowed as the variation of the magnetic field in direction of the current flow is low compared to the field change perpendicular to the current flow. The total number of elements for the displayed mesh is 278595. The corresponding number of nodes is 655277.

4.3.5. Boundary Conditions and Excitation

For the analysis of the coil, several boundary conditions are necessary. There are two main types of boundary conditions. Magnetic and electric boundaries. At the two symmetry areas of the coil model, the boundary condition *flux parallel* is applied. This boundary condition forces the magnetic flux to be parallel to the applied surface. Since the current flow is crossing the surface perpendicular, the magnetic flux at this area has to be parallel to the surface.
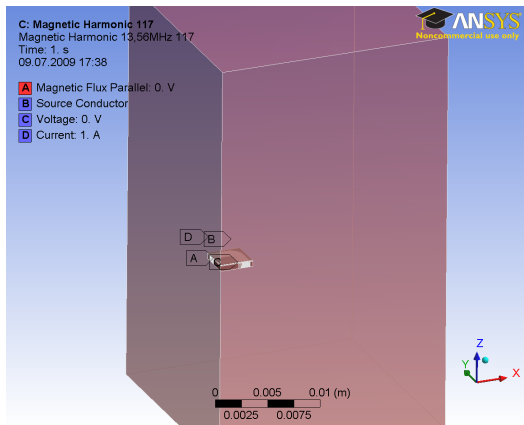
(a) Flux parallel at the surrounding areas   (b) Conductor definition and current excitation
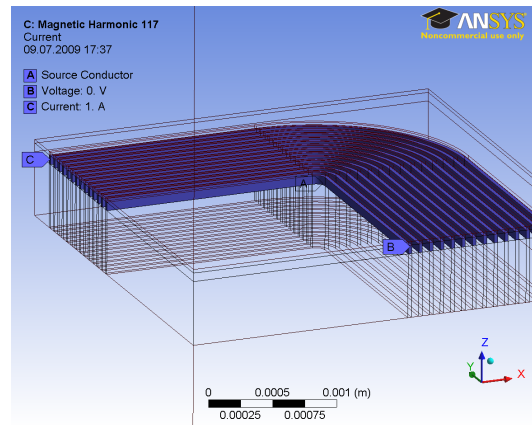
Figure 4.7.: Boundary Conditions

Additionally to the symmetry areas a boundary condition at the surface areas has to be applied. The best way would be to apply an *infinite* boundary such that the magnetic field in the model is not influenced by the modelled "air surface". For the magnetic edge elements in Ansys there is no infinite boundary available. Hence the

magnetic flux parallel condition is applied to the "air surface". Figure 4.7(a) on the facing page shows the flux parallel boundary condition applied to all exterior surfaces, including the symmetry surfaces.

The solid 117 element has the possibility to switch on or off the VOLT degree of freedom. In current carrying regions the VOLT DOF has to be switched on. The model is therefore meshed with different element properties. One for the magnetic regions without current and one for the magnetic regions with current flow. Due to this fact, in the ANSYS Workbench the current carrying regions have to be declared as *conductors*. Figure 4.7(b) on the preceding page shows the coil windings, declared as a *conductor*. The conductor needs electrical boundary conditions in addition to the magnetic boundary conditions. The current shall follow the path defined through the coil windings. This is achieved by feeding a current into the beginning of the outermost winding (see figure 4.7(b) on the facing page). The innermost winding then is "grounded" by setting the VOLT DOF to zero. The single windings are then connected with each other by coupling the VOLT DOFs.
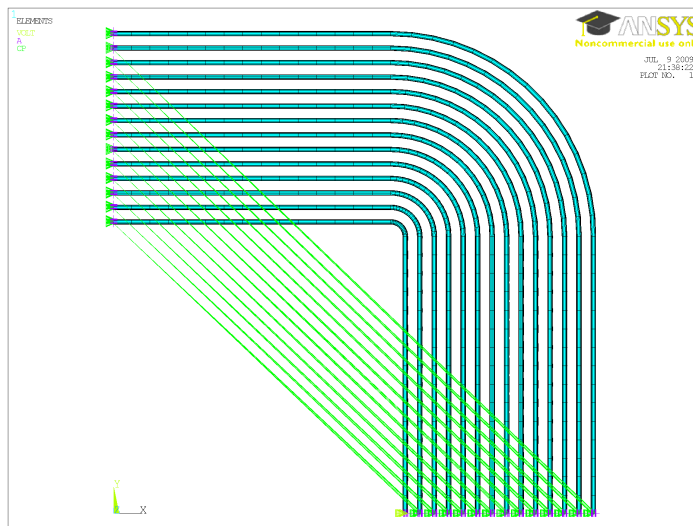
Figure 4.8.: Coupling of the VOLT DOF to connect the windings

Figure 4.8 illustrates the coupling of the VOLT DOF. This boundary condition is true for the current flow but not for the electric potential in the conductor. In reality the current has to flow trough a lossy conductor and the electric potential decreases from one side to the other. As stated before, for the magnetic field calculation this boundary conditions hold. The APDL[2] code for the coupling is listed in the appendix D on page 95.

---

[2]Ansys Parametric Design Language

4.3.6. Derivation of the Calculation Objective

As mentioned in the beginning of this chapter, the calculation objective is the coil inductance L and the coil resistance R_L. The excitation of the coil is done by applying a current of $1\,\text{A}$. The current load is added as the real part $= 1$ and the imaginary part $= 0$. This means, that at $\omega t = 0$ the current value is $1\,\text{A}$. The harmonic solution therefore calculates the VOLT degree of freedom for the current fed nodes. By using the current and voltage value, the resistance and inductance of the quarter coil model can be calculated. What has to be considered here, is that the VOLT DOF, when using the harmonic solid 117 element, represents the time integrated electric potential. Here denoted as $V(r)$ (complex quantity) and $v(r,t)$ (time dependent quantity). To reach the real electric potential $U(r)$ respectively $u(r,t)$, the results have to be differentiated.

$$v(r,t) = V_r(r)\cos(\omega t) - V_i(r)\sin(\omega t) \tag{4.4}$$

$$u(r,t) = \frac{dv(r,t)}{dt} = -\omega V_i(r)\cos(\omega t) - \omega V_r \sin(\omega t) \tag{4.5}$$

Hence the electric potential in complex form can be expressed as

$$U(r) = -\omega V_i(r) + j\omega V_r(r) \tag{4.6}$$

We therefore arrive at the real and imaginary part for the electric potential

$$U_r(r) = -\omega V_i(r) \tag{4.7}$$

$$U_i(r) = \omega V_r(r) \tag{4.8}$$

The resistance and the inductance can now be calculated using the real and imaginary part of the impedance $Z(r) = U(r)/I(r)$

$$R = \frac{U_r I_r + U_i I_i}{I_r^2 + I_i^2} \tag{4.9}$$

$$L = \frac{U_i I_r - U_r I_i}{\omega(I_r^2 + I_i^2)} \tag{4.10}$$

The derivations shown above, are executed in the simulation using APDL commands. The code is available in the appendix D on page 95.

4.3.7. Solution and Solver

The Ansys Workbench R12.0 does not support the harmonic magnetic analysis natively. The correct element types, boundary conditions and solution options have to be controlled by APDL commands inserted in the Workbench project. Appendix D

on page 95 shows the necessary commands for a harmonic analysis using the solid 117 element. If enough physical memory is available, the solution can be obtained using a direct sparse matrix solver running "in core". That is, the I/O-access to the hard disk is reduced to a necessary minimum. The 3D model was set up on a Windows XP 64bit version. The solution time for the model, (278595 elements) solving on two 3 GHz Intel Xeon cores is 493 s. The used physical memory is about 6650 MB.

4.3.8. Results and Verification

Figure 4.9(a) displays the calculated time integrated potential VOLT on the conductor surface. The maximum value occurs at the nodes where the current is applied. The minimum value of zero occurs at the nodes where the time integrated potential is set to zero. Between these points, the electric potential decreases respectively increases nearly linear.
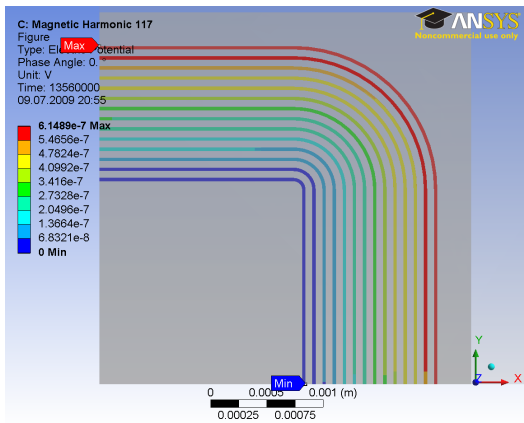
(a) Time integrated potential (real part)
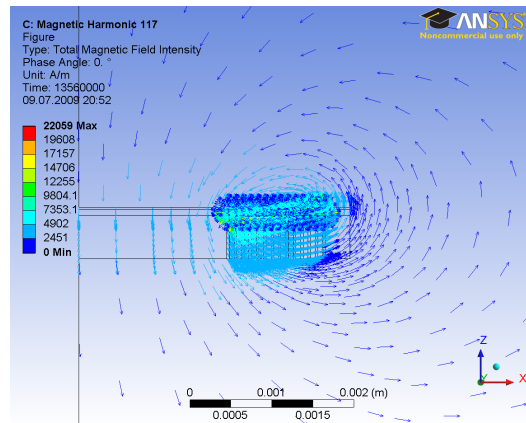
(b) Magnetic field intensity vector H
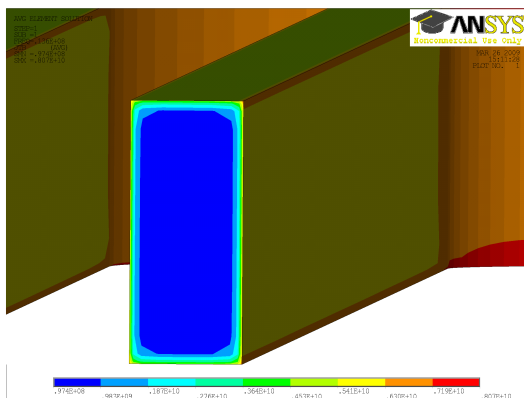
(c) Amplitude of current density J ($\sqrt{J_r^2 + J_i^2}$)
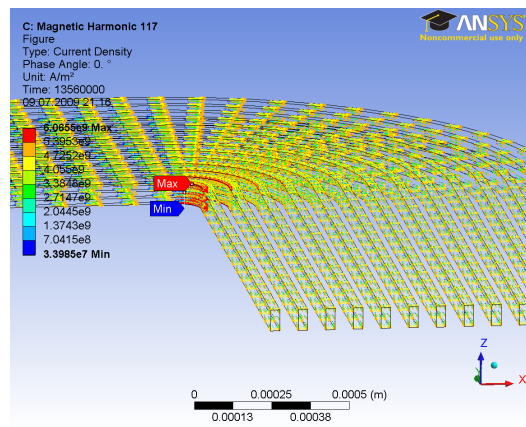
(d) Conduction current density (real part)

Figure 4.9.: Simulation results at 13.56 MHz

49

For a plausibility check of the simulation results, the magnetic field intensity is shown in figure 4.9(b) on the previous page. Displaying the field intensity vectors, illustrates the "flux lines" of the magnetic field. The route of the flux lines fits the expected empirical route. In figure 4.9(d) on the preceding page and 4.9(c) on the previous page the calculated current density in the conductor is displayed. Due to the high frequency and the high relative permeability of the conductor material, the current is mostly flowing on the conductor surface. The magnetic flux is mainly concentrated inside the conductors.

Calculated Results

As mentioned in the beginning, the calculation objectives are the coil inductance L and the coil resistance R_L. The way of obtaining the results is presented in section 4.3.6. The calculated results are

$$R = 82.085\,\Omega$$
$$L = 2.4595\,\mu\text{H}$$

Comparison with IGTE Results

For verification of the simulation method, the problem was solved by the IGTE[3] department at the Technical University of Graz. The IGTE department has developed an in-house code for the calculation of electromagnetic fields (EleFanT3D[4]). EleFanT is applicable for two and three dimensional electromagnetic field calculations. [Bir99] [PBB+95]

Figure 4.10 shows the model created by the IGTE group. The mesh is based on hexahedral elements. The excitation of the coil is done by using "racetrack" coils. The coils carry the current for the magnetic field excitation. The current density result from IGTE are shown in figure 4.10(c) on the facing page. The figure displays the magnitude of the current density in the conductor. From the IGTE model the following results are obtained:

$$R = 77.7\,\Omega$$
$$L = 2.5318\,\mu\text{H}$$

Table 4.2 on the next page compares the results gathered with the Ansys simulation software and the results calculated by the IGTE group.

Comparing the results from Ansys simulation software with the results from the IGTE group shows a 3 % difference for the calculated inductance. The resistance values differ

---

[3]Institute for Fundamentals and Theory in Electrical Engineering
[4]ELEctromagnetic Field ANalysis Tool

(a) Mesh from IGTE

(b) Excitation through racetrack coils (IGTE)

(c) Conductor current density (IGTE)

(d) Conductor mesh (IGTE)
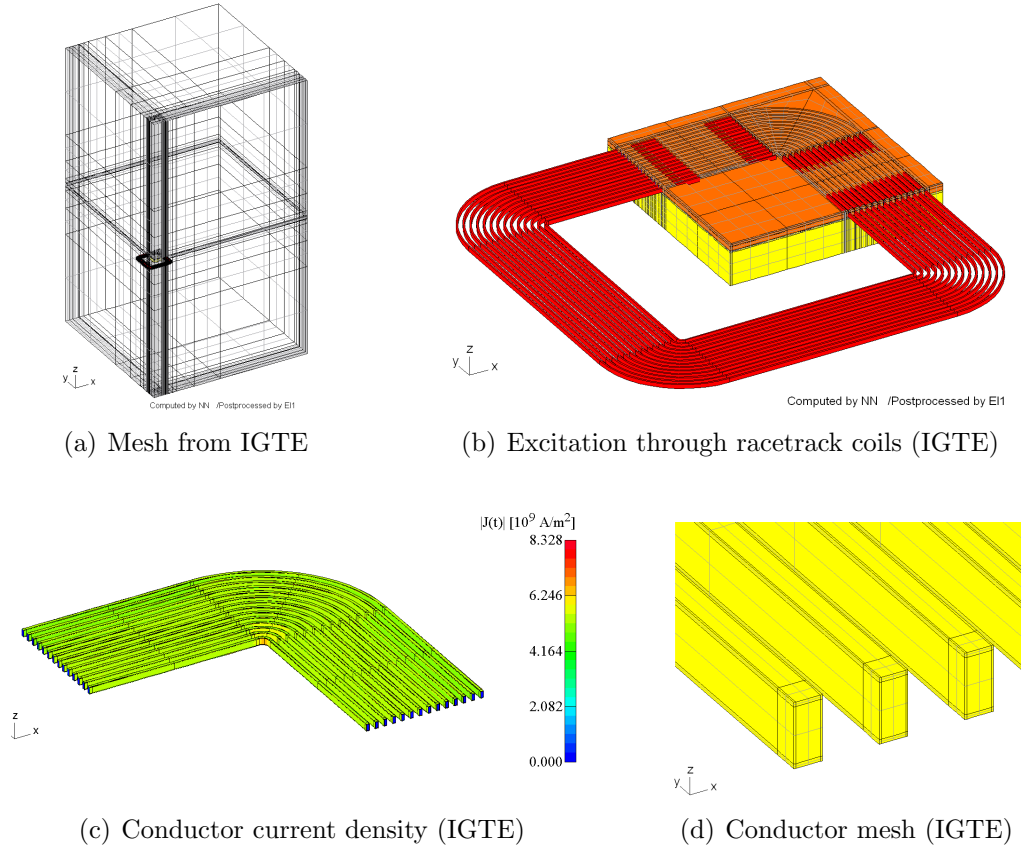
Figure 4.10.: Model calculated at the IGTE department

Table 4.2.: 3D result comparison

Quantity	IGTE	ANSYS	Deviation
R_L	$77.7\,\Omega$	$82.085\,\Omega$	$6.5\,\%$
L	$2.5318\,\mu\text{H}$	$2.4595\,\mu\text{H}$	$2.9\,\%$

more. The resistance calculated by Ansys is about $6\,\%$ higher than the result from the IGTE department. The reasons for the deviations in results can be the different meshes and the different simulation approaches. Unlike in Ansys, the simulation from the IGTE department considers the electric flux density in the insulation materials. Figure 4.10(c) displays the results for the current density in the conductor. Comparing the current density in the conductor and the displacement current shows that the current density in the conductor is 15 orders of magnitude higher than the current density in the non conducting regions. Hence, neglecting the electric flux density cannot be the reason for the difference in results. The second possibility for the deviations is the mesh. The mesh used for the Ansys simulation and the mesh generated at the IGTE are not the same. Especially the mesh in the conductor has a strong influence on the results. Figure 4.10(d) shows the mesh used for the IGTE calculations. A change

in the conductor mesh influences the resistance result stronger than the inductance result. The mesh generated by IGTE is coarser than the mesh used in the Ansys simulations (see figure 4.6(c) on page 45). Also the circular regions of the conductor are meshed finer in the Ansys simulations. Reducing the number of elements in the Ansys conductor mesh leads to a lower resistance value R_L. The different mesh therefore is one reason for the deviation in resistance results. The reason for the inductance deviation is not clear at this point. The IGTE simulation was solved using an iterative solver. Changing the convergence criteria may change the inductance results from the IGTE simulations. The elements used at the IGTE institute are second order elements whereas the solid 117 element has straigt edges and implements a linear function.

Comparison with Analytical Expressions

Analytical and empirical expressions exist for various coil geometries. [MdMHBL99] presents simple expressions for planar spiral coil geometries. The present coil geometry is approximated by the rectangular coil geometry shown in figure 4.11. According to
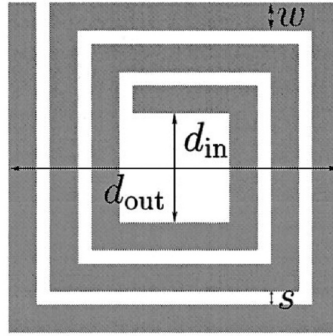
Figure 4.11.: Square coil layout [MdMHBL99]

[MdMHBL99] the inductance calculated by the modified Wheeler formula is given by:

$$L_{mw} = K_1 \mu_0 \frac{N^2 d_{avg}}{1 + K_2 \rho} \tag{4.11}$$

Where the fill factor ρ is calculated by $\rho = {(d_{out} - d_{in})}/{(d_{out} + d_{in})}$ and the average diameter by $d_{avg} = 0.5(d_{out} + d_{in})$. The coefficients K_1 and K_2 for the square coil layout are given by $K_1 = 2.34$ and $K_2 = 2.75$. μ_0 is the free space permeability and N the number of windings. In addition to the modified wheeler expression an expression based on the current sheet approximation is presented in [MdMHBL99]:

$$L_{cs} = \frac{\mu_0 N^2 d_{avg} c_1}{2} \left(\ln({c_2}/{\rho}) + c_3 \rho + c_4 \rho^2 \right) \tag{4.12}$$

The coefficients c_1, c_2, c_3 and c_4 for the square coil layout are given by $c_1 = 1.27$, $c_2 = 2.07$, $c_3 = 0.18$ and $c_4 = 0.13$. [MG68] presents an expression for the inductance calculation of rectangular planar coils:

$$L_{gr} = \frac{\mu_0}{\pi} N^2 s_1 \left[\ln \frac{2s_1 s_2}{Na(s_1 + q)} + \frac{s_2}{s_1} \ln \frac{2s_1 s_2}{Na(s_2 + q)} \cdots \right.$$
$$\left. + \frac{2q}{s_1} + \frac{0.45Na}{s_1} - \left(1 + \frac{s_2}{s_1} \right) \left(0.5 - \frac{0.5}{N} \right) \right] \tag{4.13}$$

Where $q = \sqrt{s_1^2 + s_2^2}$. s_1 and s_2 are the middle length and width of the rectangular coil. In case of the square layout s_1 equals s_2 and $s_1 = s_2 = d_{avg}$. a is the distance between the conductors and given by $a = w + s$. d is the conductor diameter (round conductor) and in this case approximated by $d = 30\,\mu m$.

Table 4.3 shows the inductance values calculated by the expressions shown before. The used input values are $d_{in} = 3.6\,mm$, $d_{out} = 6\,mm$, $w = 30\,\mu m$, $s = 60\,\mu m$, $N = 14$. Comparing the results from the analytical expressions with the results from the finite element simulation shows that the results differ about $50\,\%$. The reason for that is the neglection of the permeability of the conductor material. Furthermore the operation frequency is neglected in the analytical expressions.

Table 4.3.: Analytical Results

Formula	L
-	μH
Wheeler (L_{mw})	1.639
Current Sheet (L_{cs})	1.627
Grundlach (L_{gr})	1.695

4.4. 2D Magnetic Field Simulation

In reality, the structure of the coil does not show a rotational symmetry because the winding route is not circular but rectangular. The 3D simulation of the coil has several disadvantages. The number of elements is very high and therefore the computational time is high. Additionally the meshing process is time consuming and until now not fully automated. The automated mesher implemented in the Ansys Workbench does not produce an adequate mesh. The user has to restrain the mesher for a high quality mesh. A fully automated model and mesh creation would allow the use of an optimization algorithm on the geometry and the materials. As meshing and model creation gets simpler in the two dimensional domain, the structure of the coil is "transformed" into an equivalent circular coil.
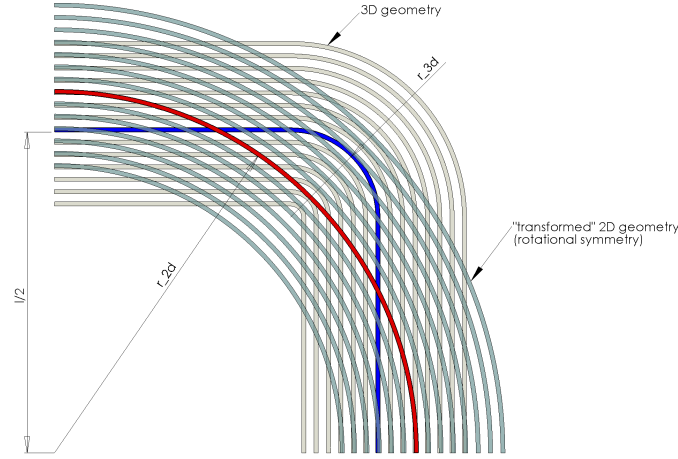
Figure 4.12.: "Transformation" from 3D to 2D domain

The circular geometry then can be modelled using 2D simulation with rotational symmetry. The rectangular coil geometry is transformed into a circular geometry by using an *equivalent* radius. The "transformation" principle is shown in figure 4.12. The equivalent radius r_{2d} is calculated based on either a constant circumference or a constant enclosed area. The circumference U of the 3D middle winding is given by

$$U = 4(l - 2r_{3d}) + 2r_{3d}\pi$$

where l is the outer lenght of the 3D coil and r_{3d} is the radius of the rounded 3D coil (see figure 4.12).

The encloseded area A of the middle 3D winding can be calculated using the following expression:

$$A = l^2 - r_{3d}^2(4 - \pi)$$

Using the upper equations, the *equivalent* 2D coil radius r_{2d} can be calculated either based on the area or the circumference of the middle 3D coil winding:

$$r_{2d} = \sqrt{\frac{A}{\pi}} \qquad \text{respectively,}$$
$$r_{2d} = \frac{U}{2\pi}$$

In the following two 2D calculations are performed to compare the difference between the area and circumference based "transformation".

4.4.1. Geometry

As the substrate material and the photoresist are not considered in the magnetic field calculation, the model reduces to the conductor and air geometry. Figure 4.13 shows

the model geometry. In the centre are the winding conductors. The inner semi circle represents the air, surrounding the conductors. The outer semi circle is necessary for the infinite boundary.
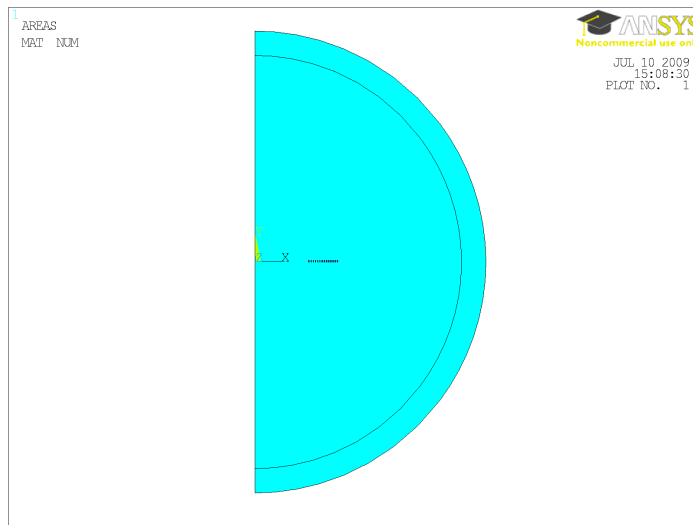
Figure 4.13.: 2D geometry (y-axis is the rotational symmetry axis)

This rather "simple" geometry can be created and meshed fully automated using Ansys APDL scripts. In appendix D on page 95 the APDL listing for the 2D magnetic field calculation can be found.

4.4.2. Analysis and Element Type

As in the 3D-simulation, eddy currents shall be considered in the 2D analysis. Ansys offers the plane 53 element for 2D magnetic field simulation considering eddy currents. The plane 53 element is based on the magnetic vector potential formulation. Details can be found in [Inc09, Theory Reference]. The element has 8 nodes carrying the vector potential **AZ** and optional the time integrated electric potential **VOLT**. Figure 4.14 shows the geometry of the plane 53 element.
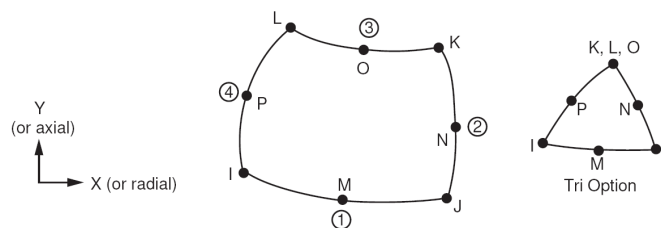
Figure 4.14.: Plane 53 element geometry [Inc09, Element Reference]

4. Simulation Method

Unlike in 3D edge based magnetic field simulations, an infinite boundary element is available for the 2D magnetic field simulation. Figure 4.15 displays the "infin 110" element. The element models an open boundary for field problems and is also applicable for the magnetic field simulation. To model the open boundary, one layer of infin 110 elements has to be modeled around the air. According to [Inc09, Element Reference] the best results are achieved when the edges connecting the inner and outer surface of the infin 110 element are radial from the model center. The edges at the open boundary have to be flagged as infinite edges.
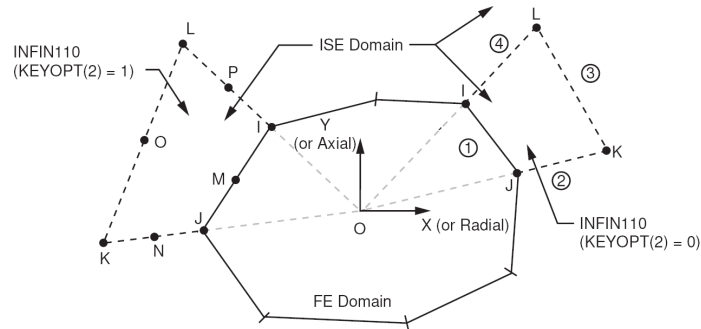
Figure 4.15.: Infin 110 element geometry [Inc09, Element Reference]

As eddy current effects shall be considered in the analysis, the analysis has to be time dependent. Like presented in section 4.3.2 on page 41 a harmonic analysis with a frequency of 13.56 MHz is performed.

4.4.3. Materials

The materials used in the 2D simulation are the same as the materials from the 3D simulation. The table containing the material parameter values can be found in section 4.3.3 on page 44.

4.4.4. Mesh

As the model geometry is generated automatically, the mesh generation can be automated. Figure 4.16 on the facing page shows the generated mesh for the 2D simulation. The mesh is generated controlling the edges on the conductor surfaces. To keep the number of elements low, the conductor is meshed coarse in the center and fine at the surface. Figure 4.16(b) on the next page shows the conductor mesh. The total number of elements for the mesh shown is 12219. The corresponding number of nodes is 36652. Compared to the 3D simulation, the number of nodes is about 18 times lower.

(a) Air mesh   (b) Conductor mesh
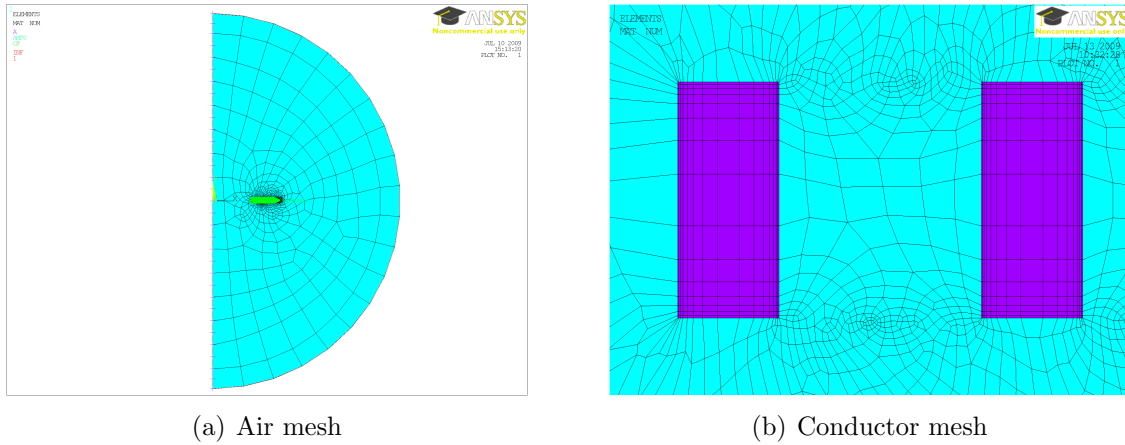
Figure 4.16.: 2D simulation mesh

4.4.5. Boundary Conditions and Excitation

Magnetic boundaries have to be applied to the exterior edges of the model. The y-axis represents the rotational symmetry axis. The magnetic boundary "flux parallel" is applied to this edge. The open boundary edges are set to be infinite edges. Figure 4.17(a) shows the magnetic flux parallel condition at the y-axis of the model and the infinite edges at the open boundary.

(a) Boundary conditions   (b) Excitation
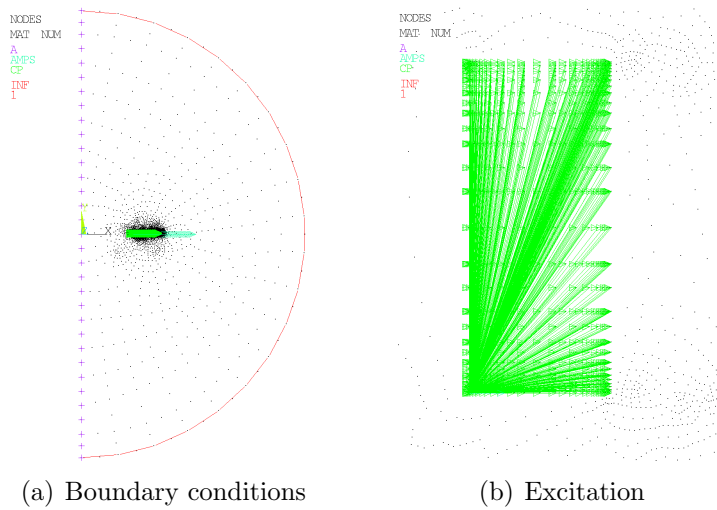
Figure 4.17.: Boundary conditions and excitation in 2D analysis

Additionally to the magnetic boundary conditions, the electric DOFs have to be constrained. The conducting areas are defined to be a solid conductor. This is achieved by coupling the VOLT DOF of the conductor nodes (see figure 4.17(b)). The excitation is applied by feeding a current of $I_r = 1\,\mathrm{A}$ into a single node of each conductor area.

4.4.6. Results and Verification

Figure 4.18(a) displays the current density vector in the conductor areas. Comparing the results with the 3D simulation (4.3.8 on page 49) shows, that the current density distribution in the conducting area is similar. Also the order of magnitude is the same.

(a) Current density (real part) (b) "Flux lines" of the magnetic field
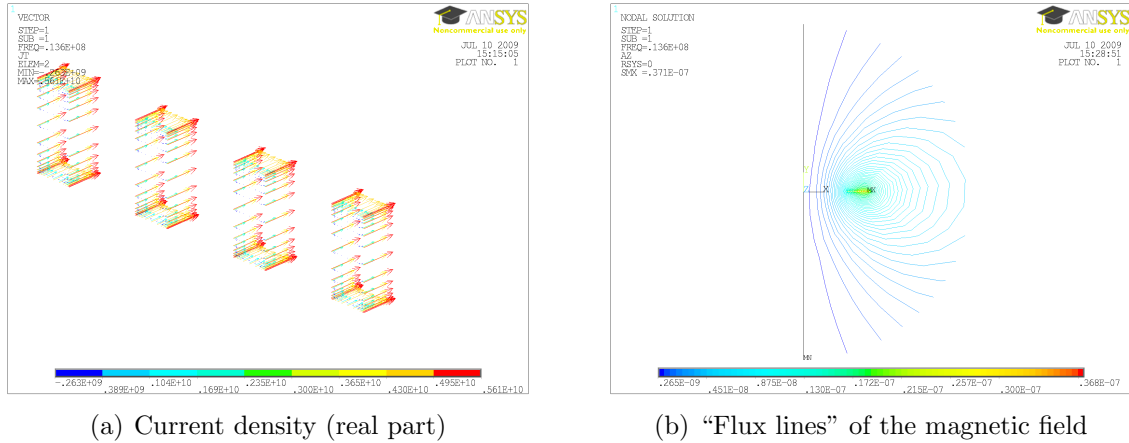
Figure 4.18.: Results from the 2D simulation

Calculated Results

Like in in the 3D simulation, the calculation objectives are the coil inductance L and the coil resistance R_L. The results are derived from the current fed into the windings and the electric potential calculated at the single windings. Summing up the electric potential at the single windings leads to the total potential loss at the coil. Using the equations derived in section 4.3.6 on page 48 the coil inductance and resistance is calculated. The results are

$$R_A = 78.87\,\Omega, \qquad L_A = 2.438\,\mu\text{H}$$
$$R_U = 84.39\,\Omega, \qquad L_U = 2.655\,\mu\text{H}$$

where R_A and L_A are the results calculated using the "area based transformation" and R_U and L_U are the results from the "circumference based transformation".

Comparison with IGTE Results

The results obtained by the IGTE department at the Technical University of Graz are listed below:

$$R = 82.5\,\Omega, \qquad L = 2.654\,\mu\text{H}$$

The results are calculated using a "circumference based trasformation". Table 4.4 compares the results obtained with Ansys and the results from the IGTE group.

Table 4.4.: 2D result comparison

Quantity	IGTE	ANSYS	
		Area based	Circumference based
R_L	$82.5\,\Omega$	$78.87\,\Omega$	$84.39\,\Omega$
L	$2.654\,\mu H$	$2.438\,\mu H$	$2.655\,\mu H$

The results from the circumference based 2D simulation agree with the results from the IGTE department. The difference in the ohmic resistance can be explained most likely due to a different mesh and the difference in calculating the 2D equvalent radius. The area based transformation delivers different results than the circumference based transformation. In the following section, the results from the 2D and 3D simulations are compared.

4.5. 2D and 3D Result Comparison

Comparing the 3D simulation results from section 4.3 with the results from the 2D simulation (see section 4.4) shows that the results for the coil resistance differ about $2.8\,\%$ to $4\,\%$. The results for the inductance calculation differ about $0.9\,\%$ to $8\,\%$. Table 4.5 summarizes the results from the 3D and 2D simulations. It can be seen, that the circumference based transformation produces better results for the resistance value. Whereas the area based transformation allows an accurate calculation of the coil inductance. The difference in the result for the inductance calculation is less than $1\,\%$.

Table 4.5.: 3D to 2D result comparison

Quantity	3D simulation	2D simulation	
		Area based	Circumference based
R_L	$82.085\,\Omega$	$78.87\,\Omega$	$84.39\,\Omega$
L	$2.4595\,\mu H$	$2.438\,\mu H$	$2.655\,\mu H$

The number of elements for the 2D simulation is about 18 times lower than used for the 3D simulation. The solution time is therefore reduced from $500\,s$ to less than one second. Therefore the "mesh density" can be chosen higher in the 2D simulation.

4.6. Electric Field Simulation

In the previous section the 3D and 2D method for the calculation of the coil inductance and the coil resistance was presented. The last calculation objective is the coil self capacitance. The capacitance can be determined by calculating the electric field, produced by the coil.

4.6.1. Geometry and Simplifications

The geometry used for the electric field simulation is displayed in figure 4.19. For the magnetic field simulations, the capacitance and chip pads were neglected. As the capacitance of the coil strongly depends on the areas of the pads, the simplification does not hold for the electric field simulation. Additionally neglecting the substrate material and the photoresist is not allowed, since they have a relative permittivity greater one. Unlike for the magnetic field analysis, no symmetry can be found for the electric field analysis. It's therefore necessary to perform a full 3 dimensional analysis considering the conductor with the pads, the photoresist and the substrate material. The main part of the electric field will concentrate around the pad areas. The relative permittivity of the substrate material is about 4 times higher than the permittivity of the air. Therefore the surrounding air needs to be modelled since the field in the air is not negligible.
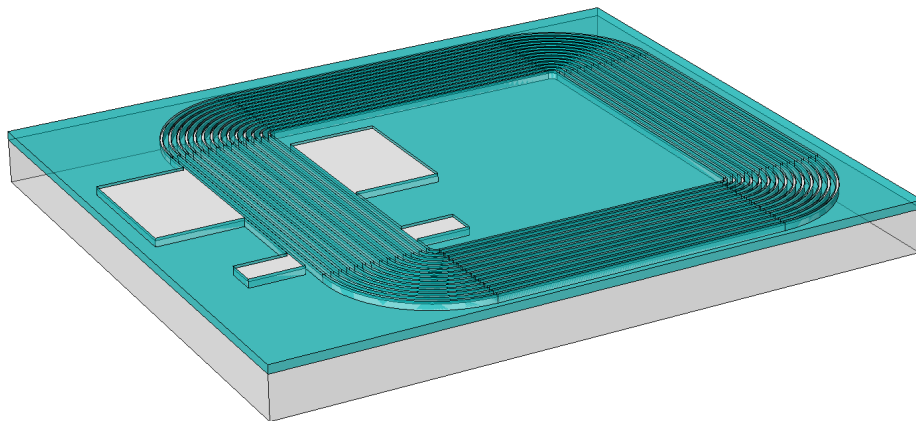
Figure 4.19.: Geometry for electric field calculation

4.6.2. Analysis and Element Type

The analysis is performed as a static electric field analysis. Ansys supports the 3D electric field analysis with the solid 231 and solid 232 elements. The solid 231 element

is a hexahedral 20 node element with the VOLT (electric potential) DOF at each node. The solid 232 is a 10 node tetrahedral element. Like the solid 231, the solid 232 calculates the VOLT DOF at each node. The solid 231 and 232 elements are current based and neglect eddy currents. The geometry of the tetrahedral element solid 232 is shown in figure 4.20. The 20 node hexahedral solid 231 is shown in figure 4.21. The Ansys Workbench Release 12.0 does not support electric field analysis. As the workbench has many advantages in meshing and geometry creation, the workbench was used for the model creation. Appendix D lists the necessary commands to change the "Workbench Magnetic" analysis into a current based electric field analysis.
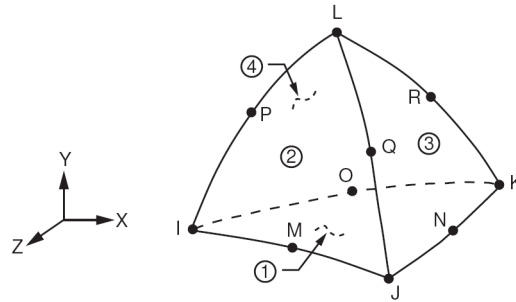
Figure 4.20.: Solid 232 element geometry
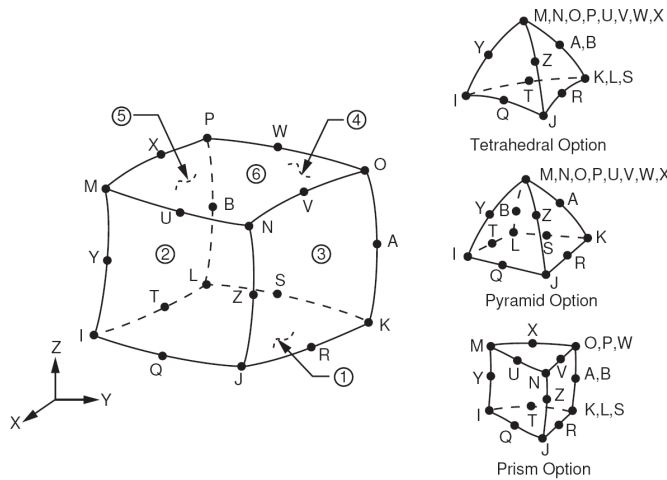
Figure 4.21.: Solid 231 geometry

4.6.3. Materials

As mentioned before, unlike the magnetic field analysis, the substrate and the photoresist need to be modelled in the electric field analysis. The materials existing in the model are nickel for the conductor, pyrex as the carrier substrate, SU-8 as photoresist

and the surrounding air. For the electric field analysis the relative permittivity ϵ_r and the resistivity ϱ need to be known. Table 4.6 summarizes the material parameters used in the model. The values for the material parameters are from the the MatWeb website `http://www.matweb.com`.

Table 4.6.: Electric material parameters

Material	ϵ_r	ϱ
-	1	$\Omega\,\mathrm{m}$
Air	1	1
Pyrex	4.1	1
SU-8	3	1
Nickel	1	6.4×10^{-8}

4.6.4. Mesh

The 3D mesh was created in Ansys Workbench Release 12.0. As eddy currents are neglected, the conductor does not need to be meshed fine in cross sectional area. This results in a coarser mesh than used for the magnetic field simulation. Figure 4.22(a) displays the meshed substrate and the surrounding air. In figure 4.22(b) the meshed coil is shown in detail. The coil wire is meshed with one element in cross section.

(a) Air mesh

(b) Meshed coil
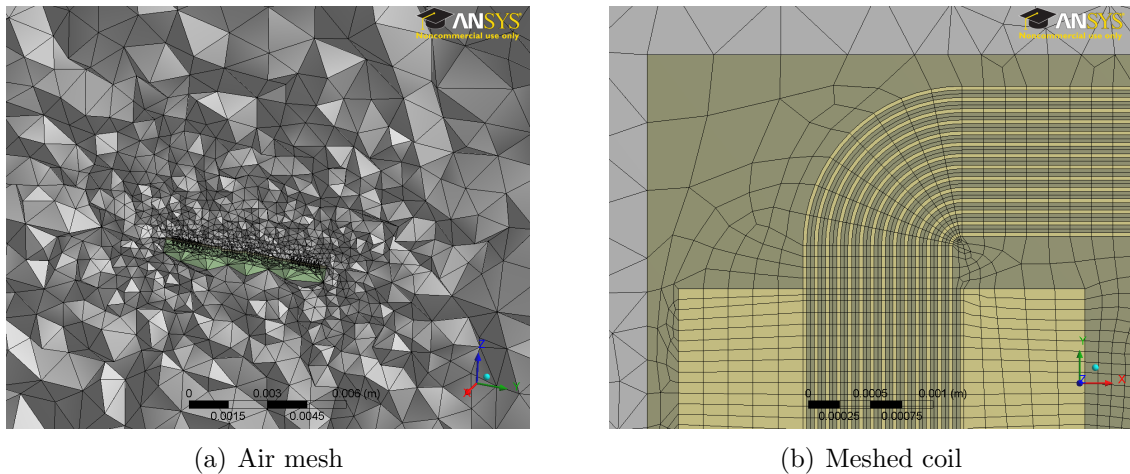
Figure 4.22.: Mesh for electric field simulation

4.6.5. Boundary Conditions and Excitation

The excitation is done by applying $0\,\mathrm{V}$ on the one side of the coil and $1\,\mathrm{V}$ on the other side of the coil. The current will flow through the conductor and result in a linear

potential decrease along the winding. This potential distribution results in an electric field.

4.6.6. Derivation of the Calculation Objective

Using the energy of the electrostatic field created by the coil, the capacitance can be derived by the following expression:

$$W_e = \frac{C \cdot U^2}{2} \tag{4.14}$$

Appendix D on page 100 lists the APDL commands for the capacitance calculation.

4.6.7. Results and Verification

Figure 4.23 displays the electric potential on the conductor, resist and substrate surface. The maximum value is 1 V at the outer chip pad and the minimum value 0 V at the inner chip pad. The actual potential distribution depends on the electric circuit in the RFID chip. As the electric circuit of the RFID chip is unknown, the boundary conditions used for this analysis are an assumption.
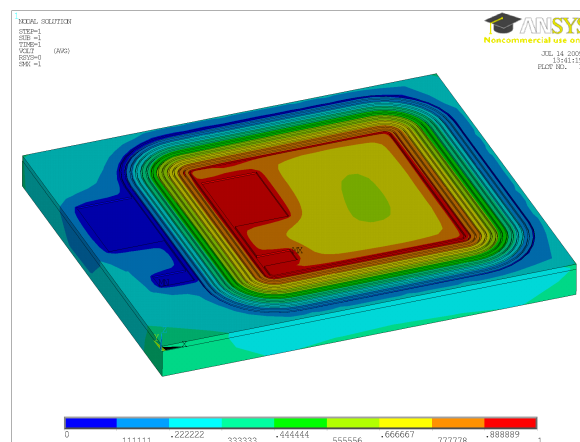
Figure 4.23.: Electric potential distribution

Result

The capacitance, calculated from the electric field energy has a value of

$$C = 0.367 \, \text{pF}$$

Comparison with IGTE result

Figure 4.24 shows the electric potential on the conductor, resist and substrate calculated by the IGTE department. The analysis from the IGTE department was performed as a quasi static electric field analysis.
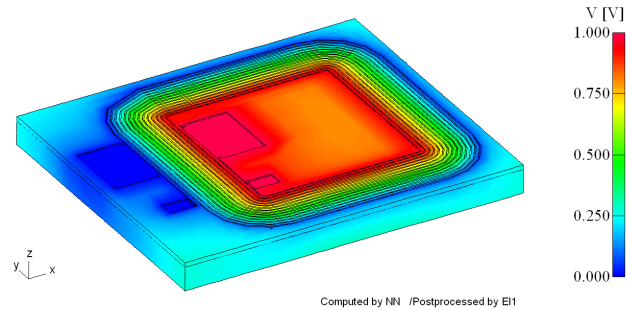
Figure 4.24.: Electric potential distribution (IGTE)

Table 4.7.: Capacitance result comparison

Quantity	IGTE	ANSYS	Deviation
C	0.351 pF	0.367 pF	4.5 %

The calculated capacitance value is $C = 0.35\,\text{pF}$. Table 4.7 compares the calculated capacitance from the IGTE group with the capacitance value calculated with Ansys. The values differ about 4.5 %. The reason for this can be the difference in mesh density or the difference in analysis type. The IGTE group treats the problem as a quasi static electric field, in Ansys the field was approximated by an electrostatic field.

4.7. Summary

During this chapter, the FEM simulation method for the characterization of the planar coil is presented. The approach is to calculate the magnetic and electric field independently. Therefore the coupling between the electric and magnetic field is neglected. The simulations were carried out using material parameters chosen from literature and can therefore not be compared with the experimental measurements. The results gathered with the Ansys program were compared with results from the IGTE institute. The comparison shows differences in the range of 3 to 6 % varying over the calculated parameters.

In the following chapter, the proposed simulation method is applied to the existing coil geometry using the material parameters, found in chapter 3. The results are then compared with the results gathered from experimental measurements.

5. Simulation Results

The simulation method as presented in the previous chapter, is applied to the existing coil geometry, using the material parameters identified in section 3.3. Additionally the geometry is modelled in more detail, according to the geometrical deviations identified in section 3.2 on page 30. Furthermore, the influence of the seed layer is investigated.

5.1. Identified Parameters

5.1.1. Material Parameters

The characterized material parameters are the relative permeability of the nickel and the resistivity of nickel. The parameter values used for the following simulations are:

$$\mu_r = 12.4$$
$$\varrho = 8.64 \times 10^{-8}\,\Omega\,\mathrm{m}$$

5.1.2. Geometry Parameters

According to section 3.2 on page 30 the actual coil geometry differs from the mask design. The deviation of the conductor thickness and the conductor height are considered in the following section.

Conductor Thickness

The nickel conductor is thinner than the designed $30\,\mu\mathrm{m}$. Measuring the conductor width (see section 3.2 on page 30) leads to an average conductor thickness of $23\,\mu\mathrm{m}$. Therefore this value is used for the following calculations.

Conductor Height

The conductor height is not constant over the winding number. That is, the inner conductor height of the sample coil is 45.96 µm and the outer conductor height 68.72 µm. From the inner to the outer winding, the conductor height increases as shown in figure 5.1.
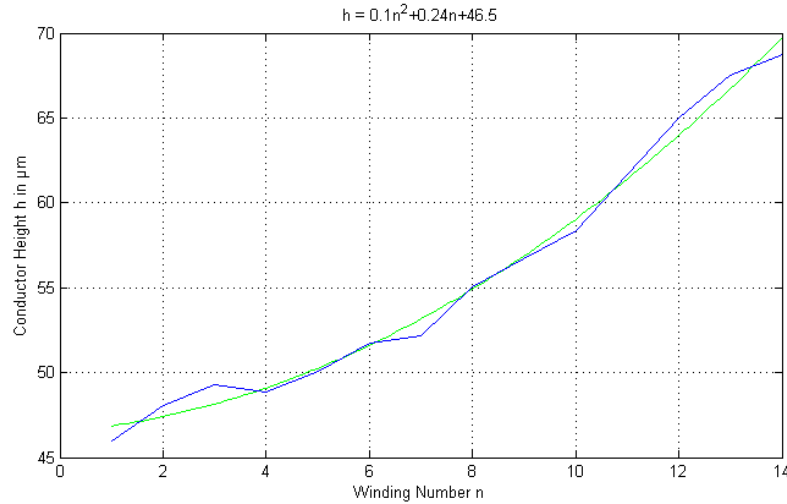
Figure 5.1.: Conductor height over winding number

The conductor heigth distribution is approximated by the polynom

$$h = 0.1n^2 + 0.24n + 46.5 \tag{5.1}$$

Where h is the conductor height in µm and n is the winding number, starting with zero for the innermost winding. The mean value for the conductor height is $\bar{h} = 55.66$ µm.

5.1.3. 2D Simulation Results

To check the influence of the non uniform height distribution on the simulation results, a 2D magnetic analysis is performed. The simulation method is presented in section 4.4 on page 53. The "area based transformation" has been used to calculate the coil radius. For the simulation with constant conductor height the mean value of $\bar{h} = 55.66$ µm is used. For the simulation with variable height the polynomial 5.1 is used to calculate the conductor height. Due to change in conductor height, the current density decreases from the inner to the outer windings. The influence on the resistance and inductance computation is less than about 0.3 %. Table 5.1 on the facing page compares the results gathered from the 2D simulation. As the change in the result for the resistance is about 0.3 % and the change in the result for the inductance is about 0.1 %, the non uniform conductor height can be approximated by using the mean value of the conductor height.

Table 5.1.: Result comparison

Quantity	Constant height	Variable height	Deviation
R_L	$17.5\,\Omega$	$17.438\,\Omega$	$0.35\,\%$
L	$1.6331\,\mu\text{H}$	$1.6313\,\mu\text{H}$	$0.11\,\%$

5.1.4. 3D Simulation Results

The previous section shows that the conductor height can be modelled using a constant height for all conductors. That is the 3D simulations are performed using a constant conductor height. This reduces the geometrical modelling effort and the number of elements. Hence the simulation time is kept low. Using the geometry parameters shown in the previous section and the material parameters explained above, the 3D simulation presented in section 4.3 on page 40 is performed.
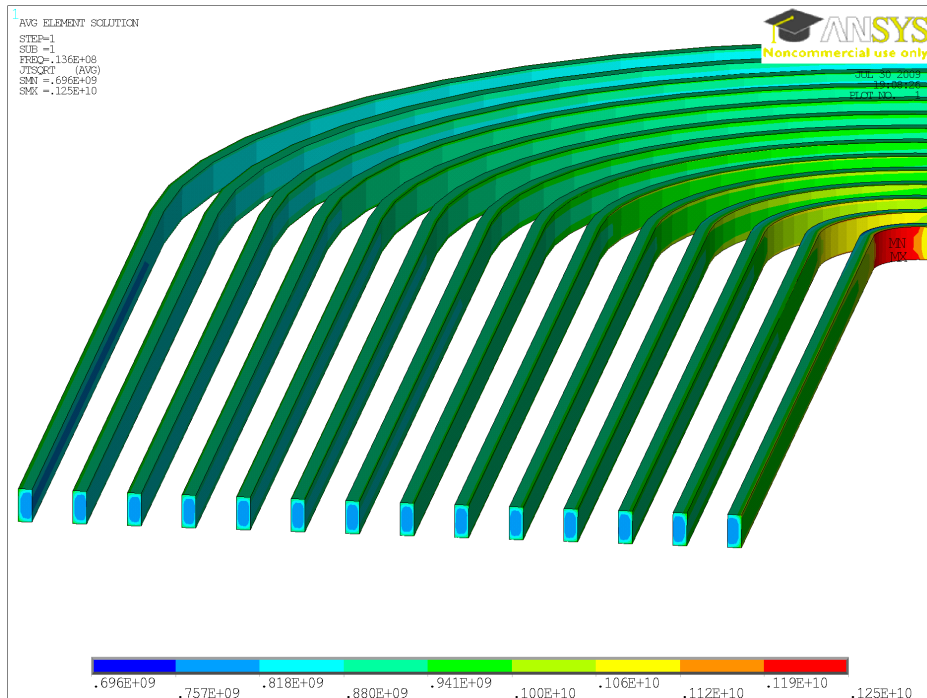
Figure 5.2.: Magnitude of current density at 13.56 MHz

Figure 5.2 shows the magnitude of the current density in the coil conductors($\bar{I} = \sqrt{I_{real}^2 + I_{imag}^2}$). Compared to the simulation results in section 4.3 on page 40, the current distribution along the conductor is uniform. This is due to the low permeability of the electroplated nickel material. The calculated resistance and inductance values are:

$$R_L = 19.163\,\Omega, \qquad L = 1.709\,\mu\text{H}$$

5.2. Seed Layer Influence

The seed layer for the electroplating process is neglected in the previous calculations. In the following, a simulation considering the seed layer is carried out to investigate the influence of the seed layer.

5.2.1. Simulation Considering the Seed Layer

The seed layer consists of a sputtered titanium and a sputtered copper layer. The thickness of each layer is 200 nm. The resistivity of copper (according to the MatWeb website) is $\varrho_{Cu} = 1.7 \times 10^{-8}\,\Omega\,\text{m}$. The resistivity of titanium is $\varrho_{Ti} = 5.57 \times 10^{-7}\,\Omega\,\text{m}$. As the resistivity of titanium is about 30 times higher than the resistivity of copper, only a 200 nm copper layer is considered in the simulation. The simulation is carried out as a harmonic 3D magnetic field simulation according to section 4.3 on page 40.

(a) Side view   (b) Isometric view
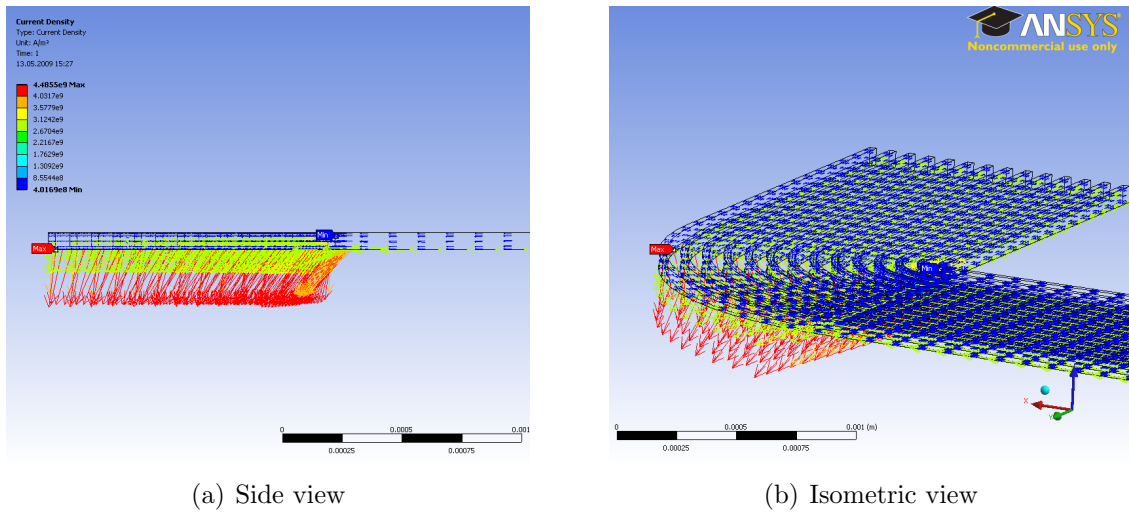
Figure 5.3.: Erroneous current density result

Figure 5.3 depicts the result for the real part of the current density. These results were calculated using the solid 117 magnetic elements. The current density shown in the figure is false for the curved part of the conductor. Whereas the current direction should follow the conductor direction, it points into the air. As the air is modelled non conductive and the displacement current is not considered, this is an erroneous result. According to [Inc09, Element Reference] the minimum allowed edge length of

the solid 117 element is 1×10^{-6}. The length unit used in the model is meters. Hence the minimum edge length equals $1\,\mu\mathrm{m}$. The seed layer thickness is $200\,\mathrm{nm}$. That is the minimum edge length of elements in the seed layer is $\leq 200\,\mathrm{nm}$. To enable the modelling of the seed layer, the solid 236 element (explained on page 41) is used. This element allows smaller edge sizes and delivers plausible results.

(a) Current density real part   (b) Current density imaginary part
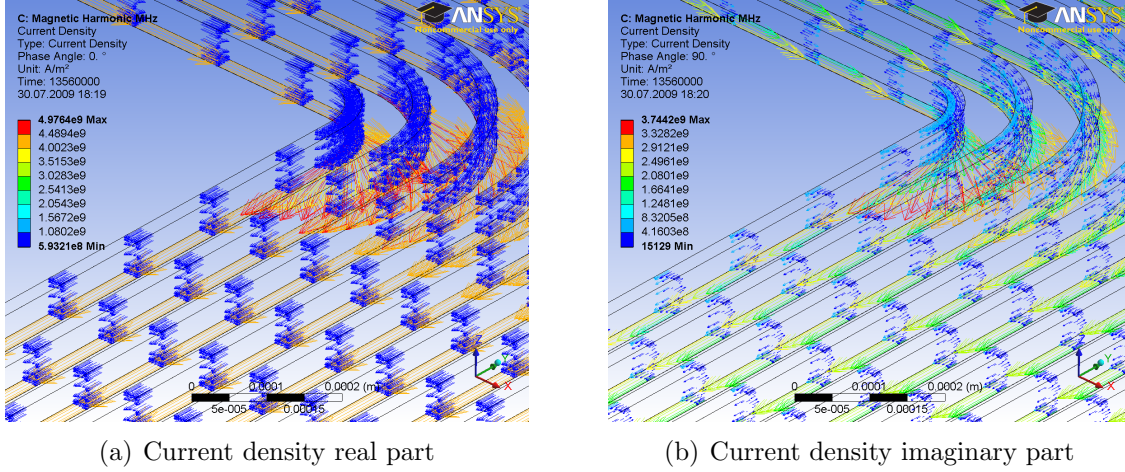
Figure 5.4.: Current density considering seed layer

Figure 5.4 shows the current density results. The current density in the seed layer is about 5 times higher than in the nickel part of the conductor. The calculated values for the coil resistance and coil inductance are:

$$R_L = 18.951\,\Omega, \qquad L = 1.7048\,\mu\mathrm{H}$$

5.2.2. Comparison

Comparing the results from above with the results from the model without seed layer (section 5.1.4 on page 67) shows that the seed layer has a larger influence on the coil resistance than on the coil inductance result. Table 5.2 shows the results for the coil resistance and coil inductance. It can be seen that the inductance result changes about $0.25\,\%$ and the resistance result changes about $1.1\,\%$.

Table 5.2.: Result comparison

Quantity	With seed layer	Without layer	Deviation
R_L	$18.951\,\Omega$	$19.163\,\Omega$	$1.1\,\%$
L	$1.7048\,\mu\mathrm{H}$	$1.709\,\mu\mathrm{H}$	$0.25\,\%$

5.3. Comparison with Experimental Results

In the previous parts the influence of model details were investigated. In this section, the results gathered from the simulations above are compared with the results from the experimental measurements. Table 5.3 summarizes the results from the simulations and the experimental measurement.

Table 5.3.: Result Comparison

Source / Simulation type	R_L	L
	Ω	μH
Coil Measurement	19.12	1.634
2D variable height	17.438	1.6313
2D constant height	17.5	1.6331
2D circumference based	18.723	1.7937
3D without seed layer	19.163	1.709
3D with seed layer	18.951	1.7048

Comparing the results from the 2D and 3D simulations with the experimental measurement results shows the deviation between simulation and measurement. Table 5.4 lists the resulting relative deiviation.

Table 5.4.: Deviation from experimental results

Simulation type	R_L Deviation	L Deviation
	%	%
2D variable height	-8.8	-0.16
2D constant height	-8.5	-0.06
2D circumference based	-2.08	9.8
3D without seed layer	0.22	4.59
3D with seed layer	-0.88	4.33

The deviation from the resistance results from the 3D simulation is less than 1%. The 3D inductance calculation error is about 4.3%. The 2D resistance calculation reaches an error of about 2% when using the "circumference based transformation". The 2D inductance calculation error is about 0.1% when using the "area based transformation".

5.4. Summary

The results gathered in this chapter show that some simplifications are valid for the calculation of the inductance and resistance values of the coils. The change in conductor height has an influence of less than 0.3% on the simulation results. Instead of

modelling the difference in conductor height, the use of a constant average height is therefore acceptable. The seed layer has an influence of less than $1\,\%$ on the simulation results. The 3D simulation resistance calculation error is less than $1\,\%$. The inductance is computed with a deviation of about $4.5\,\%$ when using the 3D simulation.

6. Discussion and Outlook

6.1. Simulation Results

The FEM technique was used to calculate the inductance L, the resistance R_L and the self capacitance C of a miniaturized planar coil. It was shown that the resistance and inductance values can be calculated using 3D- respectively 2D-magnetic field simulations. The values for the coil inductance and coil resistance can be predicted with an accuracy of about 5 %. The following table summarizes the deviations from the measured values.

Table 6.1.: Deviation from experimental results

Simulation type	R_L Deviation %	L Deviation %
2D variable height	-8.8	-0.16
2D constant height	-8.5	-0.06
2D circumference based	-2.08	9.8
3D without seed layer	0.22	4.59
3D with seed layer	-0.88	4.33

Table 7.1 on page 81 lists the results for the coil inductance and the coil resistance values. The values result either from the measurements or from different simulations. The *2D variable height* considers the non uniform conductor height and was performed as a 2D magnetic field simulation. The *2D constant height* uses a mean value for the conductor height instead of modelling the difference in conductor height. Comparing the results from this simulations shows that the change in conductor height can be approximated by using a mean value. This approximation influences the simulation results less than 0.3 %. The previous two 2D simulations were transformed from 3D to 2D using a area based transformation (see section 4.4 on page 53). By contrast the *2D circumference based* simulation results were calculated using a circumference based transformation. The results show that the circumference based transformation results in more accurate resistance results. The inductance value is calculated more precisely by using the area based transformation. The simulations *3D without seed layer* and *3D with seed layer* were performed as a 3D magnetic field simulation. The difference is the 200 nm thick copper seed layer for the electroplating process. This layer of copper remains in the coil. Comparing the results from the two simulations, it

can be seen that the influence of the copper seed layer on the simulation results is less than about 1 %. The influence on the inductance result is 0.25 %. Comparing these simulation results with the results from the experimental measurements, it is shown that the resistance value is calculated with an error of less then 1 % using the 3D simulation method. The error of the 3D inductance calculation is less than 4.5 %. The inductance error from the 2D simulation results is lower than from the 3D simulation. This seems to be implausible but becomes clear when considering that the 3D geomtry has to be transformed to an 2D equivalent radius. This transformation influences the results strongly. Hence, the precision of the 2D results is strongly dependent on the equivalent radius calculation and may be that accurate by chance.

The calculated coil self capacitance has a value of $C = 367\,\text{fF}$. Until now it was impossible to measure the coil self capacitance in a reliable way. An improved test fixture has to be built for the resonance frequency measurements and the high frequency capacitance measurements.

6.2. Further Miniaturization

The simulation method applied in this work will be used in the "Interreg IVA" project "MiniTel" (see http://www.interreg.org/. This project investigates the further miniaturization of the RFID tag and the use of the coil as a wireless sensor antenna. The actual coil size is $6\,\text{mm} \times 6\,\text{mm}$. The next miniaturization step targets a coil geometry of about $3\,\text{mm} \times 3\,\text{mm}$. Figure 6.1 on the next page shows, that for further miniaturisation the discrete capacitance has to be eliminated. This can be achieved by either avoiding the capacitance or integrating it into the coil design.

An integration of the capacitance into the coil design could be realized by adding an additional isolated electrode to the design. Figure 6.2 on page 76 shows two possibilities of including the matching capacitance into the coil design by adding a conducting and isolating layer. The figures show a cross section of the coil. Figure 6.2(a) on page 76 shows a capacitance created by a isolated conductor. The difference to the present coil is an additional conducting layer under the pads and the coil windings. Applying the conducting layer and an insulation under the pads leads to a capacitance. The insulation between the coil and the conducting bridge acts as a dielectric, the conducting bridge as a center electrode. The electric potential arising at the bridge will be half of the potential difference between the outer and inner connection pad. To estimate the capacitance value, a plate capacitor with an electrode area of $A = 1\,\text{mm}^2$ is assumed. The thickness and the relative permittivity of the dielectric are assumed to be $d = 200\,\text{nm}$ and $\epsilon_r = 4$. Using the capacitance equation for a plate capacitor a capacitance value of $C = 177\,\text{pF}$ is reached. The discrete matching capacitor has a value of $68\,\text{pF}$. Hence, it should be possible to replace the discrete capacitor by integrating the capacitance into the coil design.
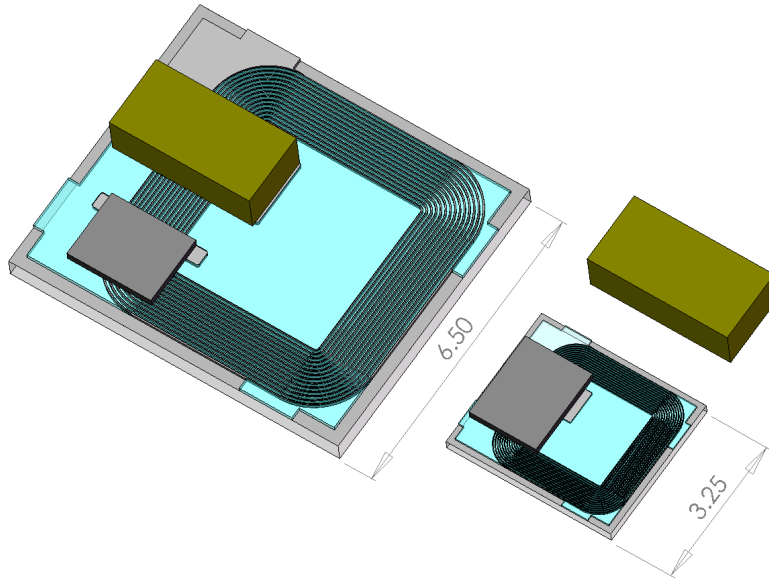
Figure 6.1.: Further miniaturization of the RFID tag

Figure 6.2(b) on the following page shows a second possibility of including a capacitance by using an electric link from the inner to the outer winding. This variant would enable a better electroplating in terms of conductor height because the inner windings are also connected during the electroplating process. Furthermore, the RFID chip can be placed in the middle of the coil or outside the coil as the connection crosses the coil windings through the conducting layer.

6.3. Changing the Conductor Material

Using copper electroplating instead of nickel electroplating would change the electric properties of the coil. Simulating the present coil with copper ($\mu_r = 1$ and $\varrho = 1.7 \times 10^{-8}\,\Omega\,\mathrm{m}$) delivers the following results:

$$R_L = 3.763\,\Omega, \qquad L = 1.6055\,\mu\mathrm{H}$$

This shows that the inductance and resistance values decrease compared to the nickel coil. Whereas the inductance decreases about $4.8\,\%$, the resistance decreases about $80\,\%$. Hence, the quality of the coil $Q = \frac{\omega L}{R_L}$ increases from $Q_{ni} = 7.7$ to $Q_{cu} = 36.4$. The higher quality results in a higher and narrower resonance curve of the resonance circuit. Hence, the voltage induced in the transponder increases and therefore the operating distance may increase. A very high quality resonance circuit requires a very stable production process. If the resonance frequency varies, it may move away from the communication side band. If it moves away too far, no data transmission is possible. The maximum quality of the coil therefore has to be adapted to the RFID

(a) Isolated seperate capacitor

(b) Capacitor by adding a jumper
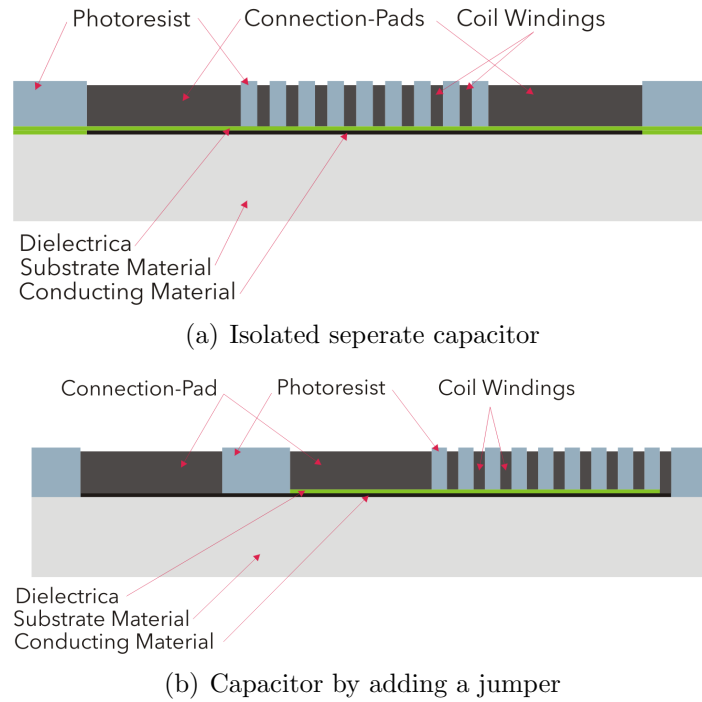
Figure 6.2.: Possibilities of realizing a matching capacitance

chip. Using copper instead of nickel as a conductor material would either result in a lower coil resistance as explained above or enable a decrease in the conductor height while keeping the resistance constant. A decrease in conductor height would enable a variation in conductor width and insulation width which would enable a change in the number of windings. Additionally the lithography process could be changed if the thickness of the photoresist can be reduced. This would allow the use of a photoresist which is easier to process than the current SU-8. This would decrease process time and complexity. Changing the electroplating process from nickel to copper opens new possibilities in variation and optimization of the design and the production process.

6.4. Further Topics

6.4.1. RFID Operating Distance

The estimation of the RFID operating distance is a complex topic. [Fin06] deals with simpflified expressions to predict the operating distance of a RFID system. Using these results and the possibilities of 2D and 3D simulations it should be possible to give statements on the influence of simulation parameter changes on the operating distance. Hence, the use of optimization algorithms on the design parameters would be interesting. In addidion to that, the coupling of the reader and tag coil could be

simulated using a magnetic field simulation. A 3D coupling simulation would require very high computational and modelling effort. The 2D and 3D results from table 4.5 on page 59 give confidence that a realistic estimation of the operating distance is possible using 2D simulations. Especially the influence of adding highly permeable materials in the reader and/or tag coil can be investigated by 2D magnetic field simulations.

6.4.2. Material Characterization

The SU-8 photoresist used as the mold for the electroplating acts as a dielectric material. The values for the permittivity and loss are given by the resist supplier. During the electroplating the resist undergoes a 18 h process with temperatures around 60 °C in an electrolyte. The influence of this process on the permittivity and the resisitivity of the photoresist have not been investigated yet. This is a subject for further work.

The permeability measurements (see section 3.3 on page 31) show a relative permeability of $\mu_r = 12.4$. Literature values for the permeability of nickel range from 20 to 1500. Hence, the electroplated nickel has a much lower permeability. The reason for this low permeability is not clear until now. Using focused ion beam (FIB) technique the nano structure of the electroplated nickel will be investigated in future work.

6.4.3. Physical Durability

When thinking about a finalized product, questions on the durability and resistance come up. Several causes for failure are possible:

- Electrical breakdown due to high resonance voltage

- Thermal breakdown due to high current density

- Failure due to harsh environmental conditions, e.g. temperature, humidity, fungal attack, etc.

- Mechanical failure due to acceleration, impact or mechanical load

To prevent these failures, the maximum environmental conditions and operating conditions have to be known. The maximum occuring current density or the maximum electric field strength could be estimated by using the simulations presented in this thesis. A prediction of the maximum operating condition can only be achieved once the maximum tolerable values for the current density and electric field strength of the used materials are known. To reach a final product, environmental conditions have to be tested according to standardized ISO or MIL tests.

7. Summary

At the Research Centre for Microtechnology (FZMT) at the Vorarlberg University of Applied Sciences working prototypes of a miniaturized planar coil for radio frequency identification (RFID) application were realized as part of the "Polyhybrid" project funded by the Interreg IIIA program of the European Union (http://www.interreg.org/). The coils were designed using empirical formulas. These formulas do not consider magnetic materials or frequency dependent effects like skin effect or eddy currents in conducting materials. Changing the substrate material from silicon to pyrex did lead to operating RFID tag prototypes after some development cycles. As the costs of development cycles are high, electromagnetic field simulations were considered to enhance the design process in future work. The aim of this thesis was to investigate the use of a commercial finite element (FEM) simulation tool to characterize the planar coils.

Experimental Characterization

The coil inductance L and the coil resistance R_L were measured using a vector network analyzer. To ensure reproducibility a special probe configuration was designed (see figure 7.1). The average measured inductance and resistance values at $13.56\,\mathrm{MHz}$ are:

$$L = 1.634\,\mu\mathrm{H}, \qquad R_L = 19.12\,\Omega$$
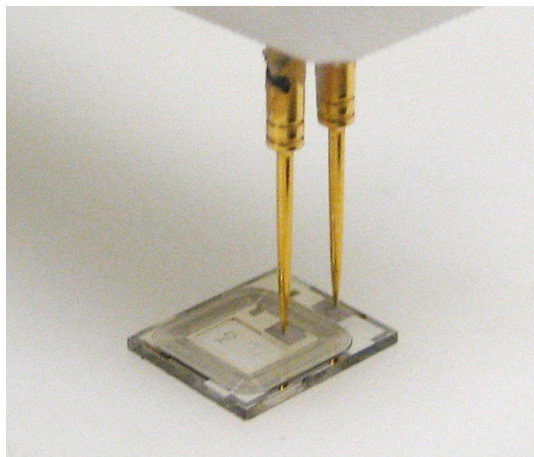
Figure 7.1.: Impedance measurement on the planar coil

The measurements were validated by comparing the obtained results with measurements from the Institute of Electrical Measurement and Measurement Signal Processing at the Graz University of Technology. The present coil is produced using a nickel electroplating process. As the material parameters of the electroplated nickel are unknown and strongly influence the simulation results, the nickel was characterized. Interestingly the measured permeability of the nickel has a value of $\mu_r = 12.4$ which is much lower than the values found in literature. They range from 20 to 1500. The resistivity of the electroplated nickel was found to be $\varrho = 8.64 \times 10^{-8}\,\Omega\,\mathrm{m}$. This is about 30 % higher than the resistivity of bulk nickel.

Simulation

The calculation objectives for the simulations are the coil inductance L, the coil resistance R_L and the coil self capacitance C. The simulations in this work have been performed as FEM simulations using the simulation program ANSYS®Academic Research, v.12.0. The calculation of the coil inductance and coil resistance was achieved by using a linear harmonic magnetic field simulation considering eddy currents. A static electric field simulation has been performed to calculate the coil self capacitance. Hence, the electric and magnetic field simulations were performed seperately and therefore no wave propagation was considered. As the wavelength of the 13.56 MHz field is $\lambda \approx 22\,\mathrm{m}$, the size of the coil geometry is about 100 times lower. Therefore the influence of the wave propagation is negligible. In order to verify the simulation method, the results obtained from the simulations were compared with simulation results from the Institute for Fundamentals and Theory in Electrical Engineering (IGTE) at the Graz University of Technology.

(a) Mesh (b) Mesh detail
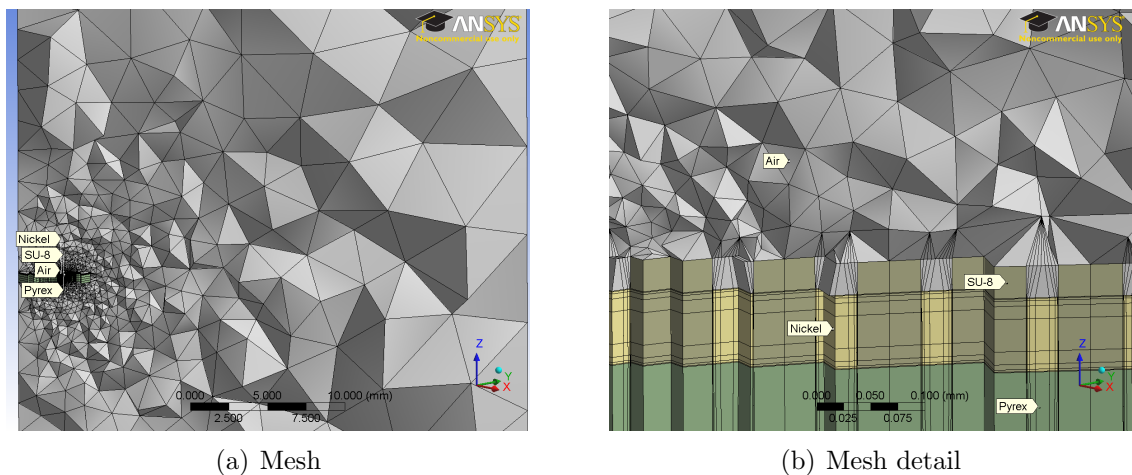
Figure 7.2.: 3D simulation mesh

Results

Using the material parameters and the exact geometrical size of the coil, the proposed simulation method delivered the results summarized in table 7.1. The coil resistance was calculated with an error less than $1\,\%$ using the 3D magnetic field simulation. The inductance value was predicted with an error of about $4.5\,\%$. The calculated coil self capacitance has a value of $C = 367\,\text{fF}$. This result has not yet been verified by measurement results.

Table 7.1.: Results

Source / Simulation type	R_L	L
	Ω	µH
Coil Measurement	19.12	1.634
2D variable height	17.438	1.6313
2D constant height	17.5	1.6331
2D circumference based	18.723	1.7937
3D without seed layer	19.163	1.709
3D with seed layer	18.951	1.7048

Outlook

The thesis shows that the electromagnetic FEM simulation is a useful tool for the characterization of the planar coil. It will be used to support the coil design process in the INTERREG IVA project "MiniTel". In this project the present coil design shall be further miniaturized and the RFID operating distance shall be increased.

Further Work

- The electric field simulations have to be verified through experimental measurements. In order to calculate the correct coil capacitance, the permittivity of the used materials has to be known. Especially the influence of the electroplating process on the material parameters of the dielectric is not known until now and necessary for a precise simulation result.

- The discrete matching capacitance necessary to trim the resonance circuit shall be replaced by a capacitance integrated in the coil design.

- The electroplating process will be changed from nickel to copper electroplating. This will reduce the coil self resistance from $\approx 20\,\Omega$ to $\approx 4\,\Omega$. The reduced resistance enables either a thinner conductor or increases the quality of the resonance circuit and will therefore have an influence on the operating distance.

- The influence of magnetic materials will be investigated using the magnetic field simulations. It may be possible to increase the operating distance by introducing ferromagnetic materials into the reader and/or tag coil design.

7. Summary

The simulation method applied in this thesis will help to solve the still outstanding problems and enable an optimization of the present coil design.

Parts of the results of this thesis are to be published in the Compumag 2009 conference proceedings and/or the IEEE Transactions on Magnetics under the title "Calculation of Equivalent Circuit Parameters for a High-Frequency RFID Transponder".

Bibliography

[AA98]   C.H. Ahn and M.G. Allen. Micromachined planar inductors on silicon wafers for MEMS applications. *IEEE Transactions on Industrial Electronics*, 45(6):866–876, 1998.

[AB03]   Jaime Aguilera and Roc Berenguer. *Design and test of integrated inductors for RF applications*. Kluwer, 2003.

[BBM+05]   M. Bensetti, Y. Le Bihan, C. Marchand, C.-M. Tassetti, G. Lissorgues, E.D. Gergam, and J.-P. Gilles. A hybrid finite-element method for the modeling of microcoils. *IEEE Transactions on Magnetics*, 41(5):1868–1871, 2005.

[Beu03]   Klaus Beuth. *Elektronik 2. Bauelemente*. Vogel, 17. edition, May 2003.

[Bir99]   O. Biro. Edge element formulations of eddy current problems. *Computer Methods in Applied Mechanics and Engineering*, 169:391–405, 199.

[BLT93]   Kenneth John Binns, Peter J. Lawrenson, and C. Trowbridge. *The Analytical and Numerical Solution of Electric and Magnetic Fields*. John Wiley & Sons Ltd, 1993.

[CMP08]   Pavlina Choleva, Roman Mathies, and Stefan Partel. Mikrogalvanik in tiefen SU-8 strukturen. In *Dornbirner Mikrotechniktage*, 2008.

[Fin06]   Klaus Finkenzeller. *RFID-Handbuch*. Hanser Fachbuchverlag, 3. edition, 2006.

[Inc09]   ANSYS, Inc. ANSYS academic research, release 12.0, help system, 2009.

[Jac98]   John David Jackson. *Classical Electrodynamics*. Wiley & Sons, 3. edition, December 1998.

[KMR08]   Karl Küpfmüller, Wolfgang Mathis, and Albrecht Reibiger. *Theoretische Elektrotechnik: Eine Einführung*. Springer, 18. edition, June 2008.

[Lab09]   Omicron Lab. Bode 100 user manual. http://www.omicron-lab.com/fileadmin/assets/manuals/Bode100_UserManual_HiRes.pdf, May 2009.

Bibliography

[Lee03]   Youbok Lee. Antenna circuit design for RFID applications. http://ww1.microchip.com/downloads/en/AppNotes/00710c.pdf, May 2003.

[Leo03]   See-Chuan Leong. Design, optimization of RF spiral inductors using scalable compact and accurate models. *Analog Integrated Circuits and Signal Processing*, 37(3):165–177, December 2003.

[LSN+04]   W.Y. Liu, J. Suryanarayanan, J. Nath, S. Mohammadi, L.P.B. Katehi, and M.B. Steer. Toroidal inductors for Radio-Frequency integrated circuits. *IEEE Transactions on Microwave Theory and Techniques*, 52(2):646–654, 2004.

[MdMHBL99]   S.S. Mohan, M. del Mar Hershenson, S.P. Boyd, and T.H. Lee. Simple accurate expressions for planar spiral inductances. *IEEE Journal of Solid-State Circuits*, 34(10):1419–1424, 1999.

[MG68]   Hans Heinrich Meinke and F.W. Gundlach. *Taschenbuch der Hochfrequenztechnik*. Springer, 1968.

[MMP08]   S. Merzaghi, P. Meyer, and Y. Perriard. Development of planar microcoils for an electromagnetic linear actuator fabricated in Batch-Type wafer technology. In *Industry Applications Society Annual Meeting, 2008. IAS '08. IEEE*, pages 1–6, 2008.

[NJS+97]   C Neagu, H Jansen, A Smith, J Gardeniers, and M Elwenspoek. Characterization of a planar microcoil for implantable microsystems. *Sensors and Actuators A: Physical*, 62(1-3):599–611, 1997.

[OWK+09]   Terence O'Donnell, Ningning Wang, Santosh Kulkarni, Ronan Meere, Fernando M.F. Rhen, Saibal Roy, and S.C. O'Mathuna. Electrodeposited anisotropic NiFe 45/55 thin films for high-frequency microinductor applications. *Journal of Magnetism and Magnetic Materials*, In Press, Corrected Proof, 2009.

[PBB+95]   K. Preis, I. Bardi, O. Biro, R. Hoschek, M. Mayr, U. Peterlini, K.R. Richter, and I. Ticar. Computer animation of electromagnetic phenomena. *IEEE Transactions on Magnetics*, 31(3):1714–1717, 1995.

[SSC08]   Kuo S-K., Chen S-L., and Lin C-T. An accurate method for impedance measurement of RFID tag antenna. *Progress in Electromagnetics Research*, 83:93–106, 2008.

List of Figures

A. Nickel Electroplating

The following tables summarize the process parameters for the nickel electroplating.

Table A.1.: Electrolyte

Ingredient	Concentration
-	$\mathrm{g\,l^{-1}}$
$Ni(NH_2SO_3)_2 \cdot 7H_2O$	70-95
$NiCl_2 \cdot 6H_2O$	10
H_3BO_3	30-40
Additive	10

Table A.2.: Process Parameters

pH	3.6-4
Temperature	48-52 °C
Current Density	$5\,\mathrm{A/dm^3}$
Deposotion Rate	$6\,\mathrm{\mu m\,h^{-1}}$

B. Measurement Results

B.1. Balanced versus Unbalanced Probe

Figure B.2 on the next page and B.1 show the results from the resistance measurements. Solid line ...device under test not rotated, dotted line...device under test rotated about 180°.
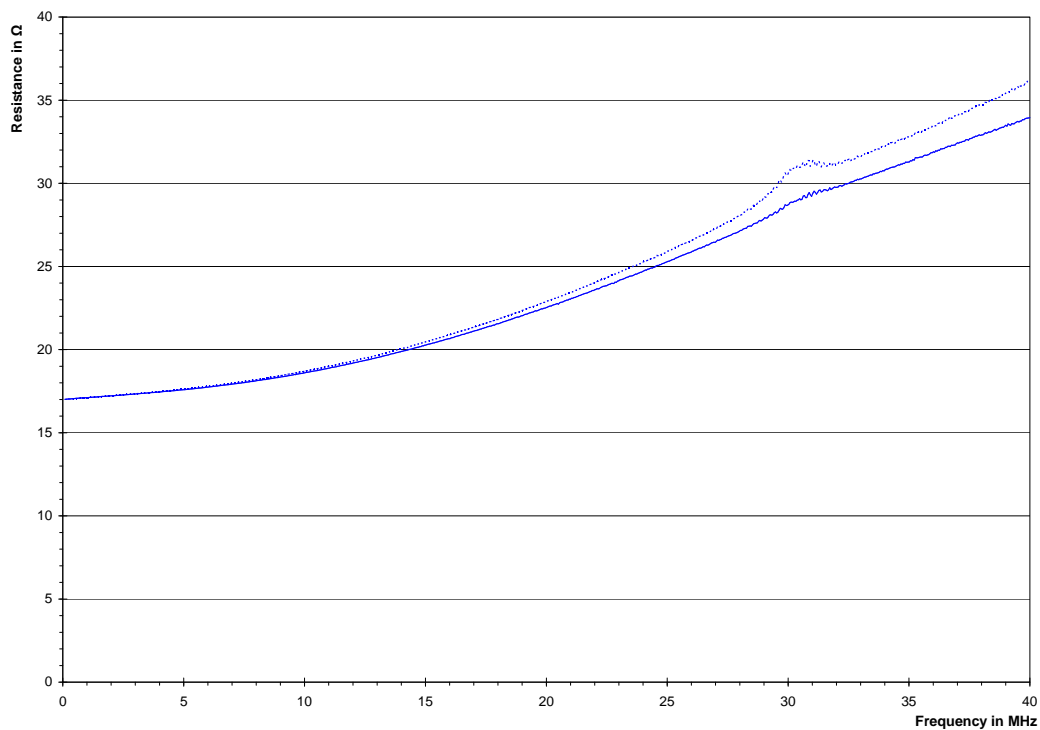
Figure B.1.: Unbalanced Probe
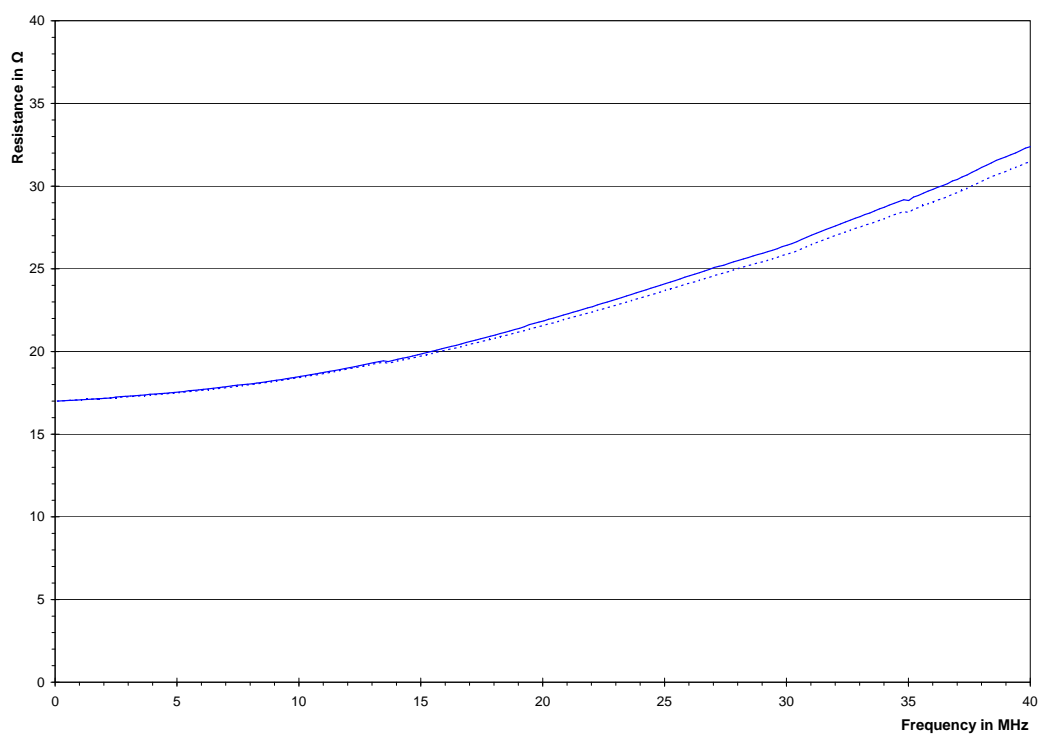
Figure B.2.: Balanced Probe

C. Error Estimation

C.1. Relative Permeability

The relative permeability is calculated using the expression

$$\mu_r = \frac{L2\pi}{N^2 \mu_0 b \ln \frac{r_2}{r_1}} \tag{C.1}$$

Hence the permeability is a function of the measuered inductance and geometrical values. The expected maximum appearing errors are listed in the following table. The inductance measurement is assumed to have a maximum error of $2\,\%$. The geometrical measurements are assumed to have a maximum error of approx. $50\,\mu$m. This is due to the reason that the geometries are not idealy and the measurements were taken using a slide gauge.

Table C.1.: Errors

Quantity	Value	Error
L	$1.6\,\mu$H	$2\,\%$
b	$1.3\,$mm	$4\,\%$
r_1	$1.85\,$mm	$3\,\%$
r_2	$5.15\,$mm	$2\,\%$

To estimate the maximum possible error (worst case) $\Delta\mu_r$, the partial derivatives are mulitplied with the error and summed up.

$$\Delta\mu_r = \left|\frac{\partial\mu_r}{\partial L}\right|\Delta L + \left|\frac{\partial\mu_r}{\partial b}\right|\Delta b + \left|\frac{\partial\mu_r}{\partial r_1}\right|\Delta r_1 + \left|\frac{\partial\mu_r}{\partial r_2}\right|\Delta r_2 \tag{C.2}$$

Using the values from table C.1 and inserting in equation C.2 we arrive at a maximum possible error of $\Delta\mu_r \approx 8.7\,\%$.

C.2. Nickel Resistivity

The resistivity of the nickel was calculated using the expression

$$\varrho = \frac{RA_{ni}}{l} \tag{C.3}$$

where A_{ni} is calculated as a trapezoidal cross section

$$A_{ni} = \frac{A+C}{2}H \tag{C.4}$$

Hence we arrive at a function for ϱ

$$\varrho = \frac{HR}{l}\frac{A+C}{2} \tag{C.5}$$

Using the partial derivatives and the approximated maximum errors from table C.2, we arrive at the equation

$$\Delta\varrho = \left|\frac{\partial\varrho}{\partial R}\right|\Delta R + \left|\frac{\partial\varrho}{\partial A}\right|\Delta A + \left|\frac{\partial\varrho}{\partial l}\right|\Delta l + \left|\frac{\partial\varrho}{\partial H}\right|\Delta H + \left|\frac{\partial\varrho}{\partial C}\right|\Delta C \tag{C.6}$$

and a maximum possible error of $\Delta\varrho \approx 7\,\%$

Table C.2.: Estimated errors for resistivity calculation

Quantity	Value	Error
R	$6.09\,\Omega$	$1\,\%$
A	$224\,\mu m$	$2\,\%$
l	$758.5\,mm$	$1\,\%$
H	$46.5\,\mu m$	$5\,\%$
C	$238.5\,\mu m$	$2\,\%$

C.3. Impedance Measurements

The Bode 100 vector network analyzer has according to the user manual [Lab09] a maximum gain error of 0.1 dB. The maximum phase error is $\Delta\varphi = 0.5°$. The gain error in percent equals

$$G_e = 100 - 100 \cdot 10^{\frac{-0.1}{20}} = 1.145\,\% \tag{C.7}$$

Using the equations for the real and imaginary part of the impedance we arrive at

$$R = r\cos(\varphi) \tag{C.8}$$

$$L = \frac{r\sin(\varphi)}{\omega} \tag{C.9}$$

$$r = \sqrt{R^2 + (\omega L)^2} \tag{C.10}$$

$$\varphi = \arctan\left(\frac{\omega L}{R}\right) \tag{C.11}$$

where R is the resistance, L the inductance, ω the angular frequency, φ the phase angle and r the magnitude of the impedance. Using the partial derivatives the maximum possible error can be calculated. The maximum possible error for the resistance measurement therefore equals

$$\Delta R = \left| \frac{\partial R}{\partial r} \right| \Delta r + \left| \frac{\partial R}{\partial \varphi} \right| \Delta \varphi = \cos \varphi \cdot \Delta r + r \sin \varphi \cdot \Delta \varphi = 1.657 \, \Omega \tag{C.12}$$

The maximum possible inductance error similarly results from

$$\Delta L = \left| \frac{\partial L}{\partial r} \right| \Delta r + \left| \frac{\partial L}{\partial \varphi} \right| \Delta \varphi = \frac{\sin \varphi}{\omega} \cdot \Delta r + \frac{r}{\omega} \cos \varphi \cdot \Delta \varphi = 0.021 \, \mu H \tag{C.13}$$

D. APDL Listings

Listing D.1: Inductance Calculation

```
1  !    Commands inserted into this file will be executed immediately after the Ansys
        /POST1 command.
2  !    Active UNIT system in Workbench when this object was created:  Metric (m, kg,
        N, s, V, A)
3
4  !arg1...Symmetry factor für Result calculation
5  symfac = arg1
6
7  /com,--- Resistance and Inductance Calculation ---
8  !********************************************************
9  ! Calculation of R and L
10 !********************************************************
11
12 cmsel,s,Current              !select the nodes where the current is applied
13 *get,nodenum,node,0,num,min
14
15 ! Real Part
16 set,1,1,1,0                  ! Read loadstep 1, first substep, scale factor 1, real
        part
17 volt_r = volt(nodenum)       ! Get time integrated voltage
18 curr_r = 1
19 alls
20
21 ! Imaginary Part
22 set,1,1,1,1                  ! Read imaginary part
23 volt_i = volt(nodenum)       ! Get time integrated voltage
24 curr_i = 0
25 alls
26
27 *afun,rad                    ! use radiant for angular expressions
28 pi=acos(-1)
29 omega = 2*pi*frequenz
30
31 ! calculate voltage out of time integratet voltage
32 voltage_r = (-omega)*(volt_i) ! real part
33 voltage_i = (omega)*(volt_r)  ! imaginary part
34
35 ! Resistance (Wirkwiderstand, effective resistance)
36 my_widerstand = symfac*(voltage_r*curr_r + voltage_i*curr_i)/(curr_r**2 + curr_i
        **2)
37 ! Reactance (Blindwiderstand)
38 my_reactance = symfac*(voltage_i*curr_r - voltage_r*curr_i)/(curr_r**2 + curr_i
        **2)
39 ! Inductance (Eigeninduktivität)
40 my_induktivitate = my_reactance / (omega)
41
42 alls
```

Listing D.2: APDL Commands for Harmonic Analysis

```
1  !    Commands inserted into this file will be executed just prior to the Ansys
        SOLVE command.
```

```
2  !     These commands may supersede command settings set by Workbench.
3  !     Active UNIT system in Workbench when this object was created: Metric (m, kg,
       N, s, V, A)
4
5  *if,flag_eddy,ne,1,then
6
7  !arg1...Frequency for harmonic analysis
8  frequenz = arg1
9
10  !/config,noeldb,0     ! force off not writing results to database
11  /prep7
12
13  !*******************************************************
14  ! Switch the element types
15  !*******************************************************
16  /com,---Switching the elementtypes and keyoptions---
17
18  cmsel,s,Leiter
19
20  *get,enum,elem,,count
21  *dowhile,enum
22   *get,etyp,elem,elnext(0),attr,type
23   et,etyp,117,1 !AZ,VOLT-switches to harmonic
24   esel,u,type,,etyp
25   *get,enum,elem,,count
26  *enddo
27  etlis
28  alls
29
30  !*******************************************************
31  ! Connecting the single windings via coupling of VOLT DOF
32  !*******************************************************
33
34  *do,i,1,13
35         cmsel,s,pair%i%
36         cp,next,volt,all
37  *enddo
38  alls
39
40  !*******************************************************
41  ! Harmonic Analysis
42  !*******************************************************
43
44  /solu
45  antype,harm
46  harf,frequenz
47
48  *endif
49  flag_eddy=1
```

Listing D.3: 2D Model

```
1  !************************************************************
2  ! 2D - Impedance calculation of circular planar coil
3  !
4  ! Author: Florian Hämmerle , 18.06.09
5  !
6  !************************************************************
7
8  finish
9  /clear
10  /prep7
11  /WINDOW,1,-1,1.67,-1,1
12
13  !-----------------------------------------------------------
14  !Parameters:
```

```
15  frequenz = 13.56e6

16

17  n_spule = 14             !No of windings
18  h_leiter = 0.07e-3       !Conductor heigth
19  airs = 5e-3              !Air size
20  b_leiter = 0.03e-3       !Conductor width
21  b_lack = 0.06e-3         !Width of insulation
22  e_size = 5e-3            !Elementsize in air
23  frequenz = 13.56e6       !Frequency of harmonic solution
24  current = 1              !1 Ampere current flow

25

26  pi=acos(-1)

27

28  !------------------------------------------------------------
29  !Calculation of 3D to 2D equivalent radius
30  r_3d = 0.63e-3  !winding rounding radius
31  l_3d = 4.68e-3  !outer size of middle winding
32  !enclosed area by the middle winding
33  a_3d = l_3d**2-r_3d**2*(4-pi)
34  !circumference of the middle winding
35  u_3d = 4*(l_3d-2*r_3d)+2*r_3d*pi

36


37

38  !Equal circumference
39  r_2d = u_3d/(2*pi)
40  !Equal enclosing area
41  !r_2d = sqrt(a_3d/pi)

42

43  !------------------------------------------------------------
44  !Geometry:
45  r_i = r_2d - (6*(b_leiter+b_lack))
46  r_a = r_i + n_spule*(b_leiter+b_lack)

47

48  wpcsys,,0
49  wpoffs,r_i

50

51  *DO,i,1,n_spule
52      rectng,0,b_leiter,0,h_leiter
53      wpoffs,(b_leiter+b_lack)
54  *ENDDO

55

56  wpcsys,,0

57

58  PCIRC,0,r_a+airs,-90,90
59  PCIRC,r_a+airs,r_a+airs+1e-3,-90,90

60

61  asel,all
62  aovlap,all

63

64  !------------------------------------------------------------
65  !Elements:

66

67  ET,1,53,0,,1 !Air

68

69  ET,2,53,1,,1 !Conductor

70

71  ET,3,110,0,1,1 !Infinite Boundary
72  !------------------------------------------------------------
73  !Materials:

74

75  !1 Air:
76  MP,MURX,1,1

77

78  !2 Conductor:
79  MP,MURX,2,1240
80  MP,RSVX,2,6.4e-8
```

```
81
82   !-----------------------------------------------------------
83   !Meshen:
84
85   alls
86   !Conductor
87   lsel,s,length,,b_leiter
88   lsel,a,length,,h_leiter
89   LESIZE, all,,,15,-20
90   asel,s,loc,y,h_leiter/2
91   type,2
92   mat,2
93   amesh,all
94
95   !Air
96   asel,inve
97   asel,u,loc,x,(r_a+1e-3),r_a+airs
98   type,1
99   mat,1
100  esize,20*h_leiter
101  amesh,all
102  asel,s,loc,x,(r_a+1e-3),r_a+airs
103  esize,1e-3
104  type,3
105  mshkey,1
106  amesh,all
107
108  !-----------------------------------------------------------
109  !Boundary conditions and loads
110
111  !Current in windings
112  *DO,i,1,n_spule
113     asel,s,loc,x,r_i+(b_leiter/2)+(i-1)*(b_leiter+b_lack)
114     esla
115     nsle
116     cp,next,volt,all
117     *get,nodenum,node,0,num,min
118     f,nodenum,amps,current
119  *ENDDO
120
121  !Flux parallel
122  alls
123  nsel,s,loc,x,0
124  d,all,az,0
125
126  !Infinite boundary
127  csys,1
128  nsel,s,loc,x,r_a+airs+1e-3
129  sf,all,inf
130
131  !-----------------------------------------------------------
132  !Solution:
133
134  alls,all
135  /solu
136  antype,harm
137  harf,frequenz
138  solve
139  finish
140
141  !-----------------------------------------------------------
142  !Postprocessing:
143
144  /post1
145  SET,1,1,,0 !Real part of solution
146  volt_r = 0
```

```
147  !Sum VOLT
148  *DO,i,1,n_spule
149     asel,s,loc,x,r_i+(b_leiter/2)+(i-1)*(b_leiter+b_lack)
150     nsla
151     *get,nodenum,node,0,num,min
152     volt_r=volt_r+VOLT(nodenum)
153  *ENDDO
154
155  SET,1,1,,1 !Imaginary part of solution
156  volt_i = 0
157  !Sum VOLT
158  *DO,i,1,n_spule
159     asel,s,loc,x,r_i+(b_leiter/2)+(i-1)*(b_leiter+b_lack)
160     nsla
161     *get,nodenum,node,0,num,min
162     volt_i=volt_i+VOLT(nodenum)
163  *ENDDO
164
165  alls
166  omega = 2*pi*frequenz
167  curr_i = 0
168  curr_r = current
169
170  !Calculate voltage out of time integratet voltage
171  voltage_r = (-omega)*(volt_i) ! real part
172  voltage_i = (omega)*(volt_r)  ! imaginary part
173
174  !Resistance (Wirkwiderstand, effective resistance)
175  resistance = (voltage_r*curr_r + voltage_i*curr_i)/(curr_r**2 + curr_i**2)
176  !Reactance (Blindwiderstand)
177  reactance = (voltage_i*curr_r - voltage_r*curr_i)/(curr_r**2 + curr_i**2)
178  !Inductance (Eigeninduktivität)
179  inductance = reactance / (omega)
```

Listing D.4: APDL Commands for Electric Field Analysis

```
 1  ! Florian Hämmerle
 2  ! 14.07.2009
 3
 4  finish
 5  /config,noeldb,0  !save results to database
 6  /prep7
 7
 8  !-------------------------------------------------------
 9  !Parameter:
10  voltage = 1.                    ! applied voltage in VOLT
11  !-------------------------------------------------------
12  !Materialdaten:
13
14  ! Material 1: Air
15  MP,PERX,1,1                     ! Relative permittivitiy (dielektrizität) of air
16  MP,RSVX,1,1                     ! Resistivity of air (infinity)
17
18  ! Material 2: Nickel
19  MP,RSVX,2,6.4e-008              ! Resistivity Ohm·m
20
21  ! Material 3: SU8
22  MP,RSVX,3,1                     ! Resistivity Ohm·m
23  MP,PERX,3,3                     ! Relative Permittivity of SU8 = 3
24
25  ! Material 4: Pyrex
26  MP,RSVX,4,1                     ! Resistivity Ohm·m
27  MP,PERX,4,4.1                   ! Relative Permittivity of pyrex = 4.1
28
29  !-------------------------------------------------------
30  alls
```

```
31  ! Delete all loads and boundaries created by workbench:
32  fdele,all,all
33  cpdele,all,all
34  ddele,all,all
35  !--------------------------------------------------
36  ! Assign materials and switch element type:
37
38  alls
39  *get,enum,elem,,count
40  *dowhile,enum
41   *get,etyp,elem,elnext(0),attr,type
42   et,etyp,231        !electrostatic element 231
43   esel,u,type,,etyp
44   *get,enum,elem,,count
45  *enddo
46
47  !convert degenerated 20 node hex- to 10 node tet-elements
48  TCHG,231,232
49
50  CMSEL,s,air
51  EMODIF,all,mat,1
52
53  CMSEL,s,conductor
54  EMODIF,all,mat,2
55
56  CMSEL,s,resist
57  EMODIF,all,mat,3
58
59  CMSEL,s,substrate
60  EMODIF,all,mat,4
61
62  !--------------------------------------------------------
63  ! Boundary conditions:
64
65  CMSEL,s,volt1
66  d,all,volt,voltage
67
68  CMSEL,s,volt0
69  d,all,volt,0.
70
71  alls
72  Finish
73
74  /solu
```

Listing D.5: APDL Commands for Capacitance Calculation

```
1  !   Commands inserted into this file will be executed immediately after the Ansys
       /POST1 command.
2  !   Active UNIT system in Workbench when this object was created:  Metric (m, kg,
       N, C, s, V, A)
3
4  !--------------------------------------------------------
5  !Postprocessing
6
7  /POST1
8  !Capacitance calculation using electric field energy
9  alls
10 etable,energy,sene
11 ssum
12 *get,energy,ssum,,item,energy
13 !Calculation of capacitance
14 Capacitance = 2*energy/(voltage**2)
15
16 finish
```